AGU PUBLICATIONS

JGR

Journal of Geophysical Research: Atmospheres

RESEARCH ARTICLE
10.1002/2015JD023182

Evaluating the advective Brewer-Dobson circulation in three reanalyses for the period 1979–2012

Marta Abalos[1], Bernard Legras[1], Felix Ploeger[2], and William J. Randel[3]

[1]Laboratoire de Météorologie Dynamique (CNRS/IPSL), Ecole Normale Supérieure de Paris, Paris, France, [2]Institute of Energy and Climate Research, Stratosphere (IEK-7), Forschungszentrum Jülich, Jülich, Germany, [3]National Center for Atmospheric Research, Boulder, Colorado, USA

Key Points:
- Common variability among estimates of the BDC in three modern reanalyses
- Qualitatively consistent BDC strengthening trends for 1979–2012 in reanalyses

Correspondence to:
M. Abalos,
marta.abalos@lmd.ens.fr

Citation:
Abalos, M., B. Legras, F. Ploeger, and W. J. Randel (2015), Evaluating the advective Brewer-Dobson circulation in three reanalyses for the period 1979–2012, *J. Geophys. Res. Atmos.*, *120*, doi:10.1002/2015JD023182.

Received 28 JAN 2015
Accepted 12 JUN 2015
Accepted article online 19 JUN 2015

Abstract Most chemistry-climate models show an intensification of the Brewer-Dobson circulation (BDC) in the stratosphere associated with increasing greenhouse gas emissions and ozone depletion in the last decades, but this trend remains to be confirmed in observational data. In this work the evolution of the advective BDC for the period 1979–2012 is evaluated and compared in three modern reanalyses (ERA-Interim, MERRA, and JRA-55). Three different estimates of the BDC are computed for each reanalysis, one based on the definition of the residual circulation and two indirect estimates derived from momentum and thermodynamic balances. The comparison among the nine estimates shows substantial uncertainty in the mean magnitude (~40%) but significant common variability. The tropical upwelling series show variability linked to the stratospheric quasi-biennial oscillation and to El Niño–Southern Oscillation (ENSO) and also reflect extreme events such as major sudden stratospheric warmings and volcanic eruptions. The trend analysis suggests a strengthening of tropical upwelling of around 2–5%/decade throughout the layer 100–10 hPa. The global spatial structure of the BDC trends provides evidence of an overall acceleration of the circulation in both hemispheres, with qualitative agreement among the estimates. The global BDC trends are mainly linked to changes in the boreal winter season and can be tracked to long-term increases in the resolved wave drag in both hemispheres.

1. Introduction

The Brewer-Dobson Circulation (BDC) is the net zonal mean transport circulation in the stratosphere and is frequently separated into an advective component (the residual circulation, characterized by tropical upwelling and extratropical downwelling) plus a component of eddy transport mainly associated with quasi-horizontal two-way mixing [e.g., *Plumb*, 2002; *Shepherd*, 2007]. An acceleration of the advective BDC is predicted in most chemistry-climate models (CCMs) as part of the response to increasing greenhouse gas (GHG) emissions, with tropical upwelling mass flux in the lower stratosphere increasing around 2–3% per decade in the 21st century [e.g., *Butchart et al.*, 2010]. The predicted trends are supported by robust dynamical mechanisms in models, involving enhanced wave drag in the subtropical lower stratosphere linked to strengthening of the upper flanks of the jets [*Garcia and Randel*, 2008; *Garny et al.*, 2011; *Shepherd and McLandress*, 2011]. Overall, CCMs have been shown to reproduce the main features of the past stratospheric climate variability and changes [e.g., *Eyring et al.*, 2006]. In particular, models are able to capture the stratospheric cooling trends observed for the last few decades [*Ramaswamy et al.*, 2001; *Randel et al.*, 2009; *Seidel et al.*, 2011; *Young et al.*, 2013], as well as the decreasing trends in ozone [e.g., *Garcia et al.*, 2007; *Randel and Thompson*, 2011]. Simulations of past trends in CCMs show an acceleration of the advective BDC of similar magnitude as the predicted future changes [*Butchart et al.*, 2010]. It has been shown that past trends are largely controlled by ozone depletion in the models [*McLandress et al.*, 2010]. Specifically, ozone depletion in the Southern Hemisphere (SH) polar lower stratosphere leads to a colder and stronger polar vortex, a delayed final warming and consequently stronger austral summer meridional circulation [e.g., *Son et al.*, 2010; *McLandress et al.*, 2010; *Polvani et al.*, 2011]. The opposite effect of ozone recovery in future simulations is partly compensated by the increasing GHG emissions [e.g., *McLandress et al.*, 2010]. Although the observed long-term changes in temperature and ozone suggest an acceleration of the residual circulation in the past decades, there is at present no confirmation of such trends in the stratosphere, mainly due to the lack of direct measurements [e.g., *Butchart*, 2014].

The concept of age of air (AoA) suggests that information on the stratospheric mass transport can be derived from observations of tracers with long lifetimes and low reactivity, which can be directly compared with CCM

results [*Hall and Plumb*, 1994; *Waugh and Hall*, 2002; *Waugh*, 2009]. The mean AoA provides an integrated measure of the net effect of all transport mechanisms on the tracers, including mean meridional advective circulation and two-way mixing. In models, the mean AoA shows a long-term negative trend throughout the stratosphere, consistent with an acceleration of the residual circulation [*Austin and Li*, 2006; *Garcia and Randel*, 2008; *Oman et al.*, 2009]. Moreover, *Li et al.* [2012] argue that modeled AoA trends for the 21st century are mainly due to trends in the advective component of the BDC, which dominate over changes in mixing. On the other hand, no conclusive evidence of long-term trends in the mean AoA has been found in observations so far. For instance, *Engel et al.* [2009] evaluate the mean AoA for 1975–2005 from balloon-borne tracer measurements in the Northern Hemisphere (NH) middle latitudes between 24 and 35 km and obtain no significant (and slightly positive) trends. *Ray et al.* [2010] further combine these balloon-borne measurements with satellite data and interpret the resulting global AoA trend pattern as strengthening of both the advective BDC and the mixing across the subtropics in the lower stratosphere (below ∼25 km) plus a weakened residual circulation above. Using improved calculations of the observationally based AoA, *Ray et al.* [2014] find good agreement with negative CCM trends in the lower stratosphere (below ∼20 km), while above ∼25 km opposite-sign trends are obtained for the NH middle latitudes. Estimates of the mean AoA for the last decade (2002–2010) based on satellite data from the Michelson Interferometer for Passive Atmospheric Sounding instrument also suggest positive trends above 24 km in the NH [*Stiller et al.*, 2012]. In that work the older air in the NH middle latitudes is considered as a result of increased recirculation due to weakening of the subtropical mixing barriers in the NH, while tropical upwelling is overall increasing. Important uncertainties have been pointed out in these observational trend results, including the limited spatial coverage (for in situ measurements), the short record (in satellite observations), and further technical aspects regarding derivation of AoA from tracer measurements [*Garcia et al.*, 2011]. Nevertheless, these constitute the only available estimates of stratospheric AoA trends from direct observations.

On the other hand, AoA has been estimated from the ERA-Interim reanalysis by *Diallo et al.* [2012], and the results show significant negative trends mostly in the SH lower stratosphere for the period 1989–2010, which are interpreted as an acceleration of the shallow branch of the circulation. In addition, they show a region of statistically significant positive trends in the NH middle latitudes above ∼25 km, in qualitative agreement with the observationally based results. This last result based on ERA-Interim data is also observed using a different transport model for the period 1990–2009 [*Monge-Sanz et al.*, 2013]. However, the picture derived from these reanalysis studies is not consistent with the deceleration of ∼5%/decade in lower stratosphere tropical upwelling in the period 1989–2011 obtained in *Seviour et al.* [2011]. In summary, there is currently significant uncertainty regarding the observed trends in the BDC, and this open question has important implications for understanding how well the present generation models represent stratospheric transport and its long-term changes.

Reanalyses are particularly well suited for climate analyses, because (1) they constitute long-term data sets with high spatial and temporal resolution and (2) they are developed maintaining an unvarying assimilation system to produce homogeneous data sets [*Rood*, 2003]. Nevertheless, temporal discontinuities in reanalyses can arise from changes in the assimilated observations. *Iwasaki et al.* [2009] compared the annual mean residual circulation in five reanalyses and observed important differences and highly noisy vertical velocities. However, the reanalyses used in that work belong to a previous generation and updated versions are currently available. Although there are still discontinuities due to bias correction by assimilated data, several aspects have been improved in the new generation of reanalyses [e.g., *Simmons et al.*, 2014]. In the present work we evaluate and compare the advective BDC in three of the major modern reanalyses, and we analyze the climate variability and trends for the period 1979–2012. In section 2 we provide a short description of the reanalyses and describe the three estimates of the BDC that are computed for each reanalysis. Section 3 presents the climatology of the nine estimates, section 4 examines the climate variability of tropical mean upwelling, and section 5 discusses the trends in tropical upwelling and in the global advective BDC. For simplicity, in the rest of the manuscript the advective part of the BDC will be often referred to as the BDC. Note that we do not use the term residual circulation in order to avoid confusion with one particular estimate (computed from the definition of the residual circulation, see below).

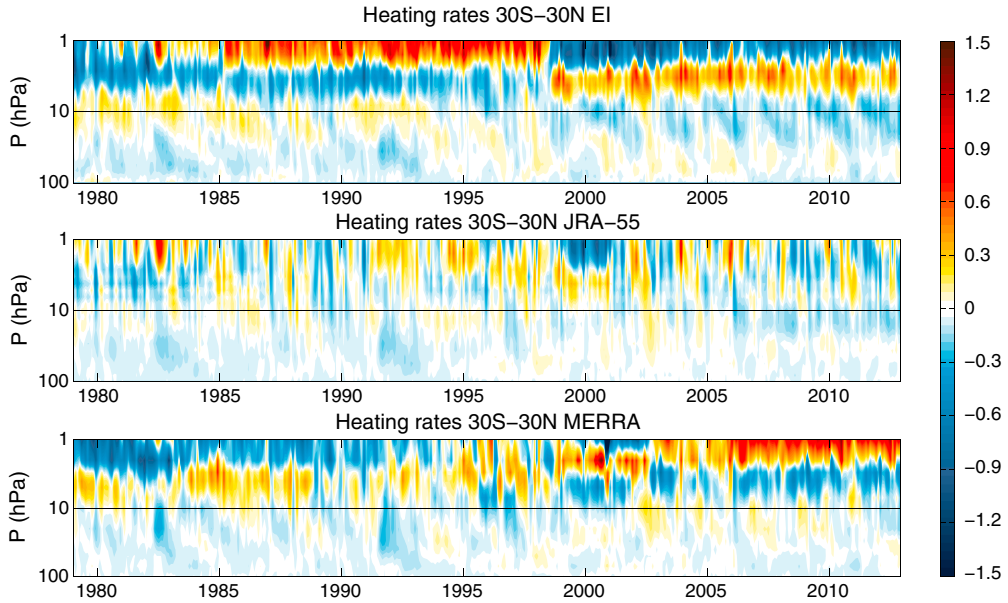

Figure 1. Monthly time series (1979–2012) as a function of altitude of deseasonalized radiative heating rates averaged over the tropical band 30°S–30°N in the three reanalyses (EI, JRA-55, and MERRA). Units: K d $^{-1}$. In order to avoid strong discontinuities in the data in the upper levels, the present study focuses on levels below 10 hPa (indicated by the black line).

2. Data and Methods

2.1. Reanalysis Data: ERA-Interim, MERRA, and JRA-55

We use reanalysis data for 1979–2012 of temperature, winds, and diabatic heating rates from ERA-Interim (Interim European Centre for Medium-Range Weather forecasts Reanalysis, denoted EI hereforth), JRA-55 (Japanese 55 year Reanalysis), and MERRA (Modern-Era Retrospective Analysis for Research and Applications). EI data is described in *Dee et al.* [2011]. It has 60 vertical levels from the surface to 0.1 hPa and a spectral resolution of T255. The 6-hourly data are provided on a regular 1° × 1° regular latitude-longitude grid, and we interpolate from hybrid model levels to the standard pressure levels. The EI reanalysis is based on a 12 h 4D-Var assimilation scheme and has a variational bias adjustment of satellite radiance data. A significant improvement in the BDC strength has been reported in EI as compared to the previous ECMWF reanalysis, ERA-40 (as shown in *Monge-Sanz et al.* [2007], for an intermediate version).

The JRA-55 is described in *Ebita et al.* [2011] and *Kobayashi et al.* [2015]. It also has 60 vertical levels spanning from the surface to 0.1 hPa and a higher horizontal spectral resolution (T319). The 6-hourly data are interpolated from hybrid model levels to the standard pressure levels. The data are retrieved on a Gaussian grid with ~0.562°spacing in longitude (640 longitude and 320 latitude grid points). The assimilation system is 4D-Var, and a new variational bias correction system helped to notably reduce the lower stratospheric temperature bias reported for the former JRA-25.

MERRA (Modern-Era Retrospective Analysis for Research and Applications) is described in *Rienecker et al.* [2011]. It is produced by the NASA Global Modeling and Assimilation Office and uses GEOS-5 assimilation system. The native grid has 72 levels up to 0.01 hPa, and a horizontal resolution of around 1/2°latitude × 2/3°longitude. However, we have used the reduced latitude grid (1.25° × 1.25°) version of MERRA 3-hourly data on pressure levels (42 levels extending to 0.1 hPa), because the heating rates are not available on the original model levels. MERRA uses a 6 h 3D-Var assimilation system and the radiance bias correction is similar to that of EI [*Simmons et al.*, 2014].

The changes in assimilated measurements in reanalyses can lead to discontinuities in the record, affecting the trends. Artificial changes in the reanalyses may arise from changes in satellite data availability, such as the replacement of TOVS (TIROS Opertional Vertical Sounder) by ATOVS (Advanced TOVS) in 1998, the end of Stratospheric Sounding Unit in 2006 and the introduction of Atmospheric InfraRed Sounder in 2002 and GPS radio occultation in 2001 (massively in late 2006), as well as the increased number of radiosonde

measurements assimilated in the last years. The recent work by *Simmons et al.* [2014] provides an accurate assessment of the long-term changes in temperature in the EI reanalysis, including some comparisons with MERRA and JRA-55. The massive introduction of GPS radio occultation measurements in late 2006 leads to warming near the tropopause in EI, while it has an opposite effect on JRA-55, due to different biases in the previous assimilated data (note that GPS data are not included in MERRA). However, the effect of such discontinuity in the reanalysis temperature trends for the period 1979–2012 is estimated to be smaller than 20% in the lower stratosphere [*Simmons et al.*, 2014]. Changes in temperature are strongly coupled with the heating rates in the stratosphere. Figure 1 shows the deseasonalized time series of the radiative heating rates in the three reanalyses as a function of altitude. Artificial discontinuities are clearly observed as abrupt changes in the sign of the anomaly. For instance, the change from TOVS to ATOVS radiance data in 1998 is clearly seen in EI and MERRA above 10 hPa (a similar feature present in JRA-25 was eliminated in JRA-55 [*Kobayashi et al.*, 2015]). The layered structure of the discontinuities is likely associated with the weighting functions of the satellite instruments. Given that these unrealistic features are notably stronger at the upper levels, where there is also a lower agreement among the reanalyses, the present work focuses on the lower and middle stratosphere below 10 hPa (~32 km).

2.2. BDC Calculations

In order to provide information on the uncertainties in the results, three independent estimates of the advective BDC are computed for each reanalysis. Because each estimate has different uncertainties and limitations, the consistency among them will provide confidence to our conclusions. The analyses are based on the Transformed Eulerian Mean framework (TEM), and the three estimates include the residual circulation definition ($\bar{v}^*, \bar{w}^*$) and two indirect estimates based on the momentum ($\bar{v}^*_m, \bar{w}^*_m$) and thermodynamic ($\bar{v}^*_Q, \bar{w}^*_Q$) balances. All calculations are based on daily mean fields computed from the 6-hourly or 3-hourly data.

The residual circulation in the meridional plane is defined as [e.g., *Andrews et al.*, 1987]

$$\begin{aligned} \bar{v}^* &= \bar{v} - e^{z/H}\left(e^{-z/H}\frac{\overline{v'T'}}{S}\right)_z \\ \bar{w}^* &= \bar{w} + \frac{1}{a\cos\phi}\left(\cos\phi\frac{\overline{v'T'}}{S}\right)_\phi \end{aligned} \tag{1}$$

where overbars denote zonal mean quantities, subscripts indicate partial derivatives, the vertical coordinate is $z = H\ln(p_0/p)$ with $H = 7$ km and $p_0 = 1000$ hPa, a is the Earth's radius, $S = HN^2/R$ is the stability parameter, where N^2 is the squared Brunt-Väisälä frequency and $R = 287$ m^2 s^{-2} K^{-1} is the gas constant for dry air. The main uncertainties in this estimate are associated with the reanalyses velocity fields (especially the vertical velocity).

We calculate the corresponding stream function $\bar{\Psi}^*$ (in kg m^{-1}s^{-1}) using

$$(\bar{v}^*, \bar{w}^*) = \frac{1}{\rho_0 e^{-z/H}\cos\phi}\left(-\frac{\partial\bar{\Psi}^*}{\partial z}, \frac{1}{a}\frac{\partial\bar{\Psi}^*}{\partial\phi}\right), \tag{2}$$

where the density is $\rho = \rho_0 e^{-z/H}$ with $\rho_0 = p_0/gH$. Hence,

$$\Psi^* = \rho_0\cos\phi\int_z^\infty \bar{v}^* e^{-z'/H}\mathrm{d}z', \tag{3}$$

where it is assumed that $\Psi^* \to 0$ as $z \to \infty$.

The second estimate of the BDC is based on the momentum balance equation

$$\bar{u}_t - \bar{v}^*\hat{f} + \bar{w}^*\bar{u}_z = \mathrm{DF}, \tag{4}$$

where $\hat{f} = f - \frac{1}{a\cos\phi}(\bar{u}\cos\phi)_\phi$, with f the Coriolis parameter, $\mathrm{DF} = \frac{e^{z/H}}{\rho_0 a\cos\phi}\vec{\nabla}\cdot\vec{F}$ is the scaled divergence of the Eliassen-Palm flux (EP flux, $\vec{F}$), and the dissipation term is neglected [*Andrews et al.*, 1987]. The following expression can be derived for the stream function corresponding to the momentum balance estimate ($\bar{\Psi}^*_m$) combined with equation (2) [*Haynes et al.*, 1991; *Randel et al.*, 2002]

$$\bar{\Psi}^*_m(\phi, z) = -\rho_0\cos\phi\int_z^\infty\left[\frac{e^{-z'/H}}{\hat{f}}\left(\mathrm{DF} - \bar{u}_t\right)\right]_{\bar{m}}\mathrm{d}z', \tag{5}$$

where the suffix $\bar{m}$ indicates that the integrand is evaluated on constant angular momentum contours. However, we perform the calculation on constant latitudes, since out of the deep tropics the angular momentum and the latitude isolines are approximately parallel. For this reason, our calculations are limited to latitudes poleward of 18°S–18°N, but we note that this simplification could constitute a source of uncertainty. The meridional and vertical components of the momentum balance estimate ($\bar{v}^*_m, \bar{w}^*_m$) are then derived using equation (2). It is important to note that equations (4) and (5) include only the eddy fluxes explicitly resolved in the reanalyses (embedded in the EP flux divergence, DF). In order to evaluate the effect of subgrid-scale waves, we have performed additional calculations including the gravity wave drag (GWD) provided by the reanalyses. This is done by adding the GWD to the resolved forcing in equation (5)

$$\bar{\Psi}^*_{m\mathrm{GWD}}(\phi, z) = -\rho_0 \cos\phi \int_z^\infty \left[\frac{e^{-z'/H}}{\hat{f}}\left(\mathrm{DF} + \mathrm{GWD} - \bar{u}_t\right)\right]_{\bar{m}} \mathrm{d}z', \tag{6}$$

While JRA-55 and MERRA directly provide the parameterized gravity wave drag (orographic and nonorographic), for EI we have used the total tendency due to physics, which should be representative of the GWD in the stratosphere.

The third estimate ($\bar{v}^*_Q, \bar{w}^*_Q$) is obtained iterating between the thermodynamic balance

$$\bar{T}_t + \frac{\bar{v}^*}{a}\bar{T}_\phi + \bar{w}^* S = \bar{Q}, \tag{7}$$

where $\bar{Q}$ are the zonal mean heating rates and the eddy term is neglected, and the mass continuity equation [e.g., *Andrews et al.*, 1987]

$$\frac{1}{a\cos\phi}\left(\bar{v}^*\cos\phi\right)_\phi + e^{z/H}\left(e^{-z/H}\bar{w}^*\right)_z = 0, \tag{8}$$

ensuring zero net mass flux across a pressure level in each iteration [e.g., *Murgatroyd and Singleton*, 1961]. The main uncertainties in this estimate are associated with the heating rates, although neglecting the eddy term may constitute an additional source of uncertainty, in particular near the tropical tropopause [see *Abalos et al.*, 2012]. We use total radiative heating rates (short plus long wave) for each reanalysis, and we limit the thermodynamic calculations to levels above 100 hPa to ensure that the total heating is dominated by the radiative heating. The stream function corresponding to the thermodynamic estimate ($\bar{\Psi}^*_Q$) is computed using equation (3).

We note that in a self-consistent model the three estimates should be identical, aside from numerical uncertainties and the mentioned approximations. However, they are not necessarily equal in reanalyses, where the differences in the data assimilation and bias correction techniques can lead to differences not only among reanalyses but also among estimates, in addition to the uncertainties described above for each estimate.

3. Climatology

Figure 2 shows the long-term (1979–2012) climatology of the BDC stream function for the nine estimates ($\bar{\Psi}^*$, $\bar{\Psi}^*_m$, and $\bar{\Psi}^*_Q$ in the three reanalyses) as a function of latitude and altitude in the region of interest. There is an overall agreement in the annual mean stream function, with positive (clockwise circulation) values in the NH and negative (counterclockwise circulation) values in the SH. In all estimates the shallow branch of the advective BDC, with downwelling at middle latitudes (streamlines reaching the tropopause around ±40–50°), can be distinguished from the deep branch, with downwelling poleward of ~60°in both hemispheres. Although the overall structure is in good agreement for the three reanalyses and all estimates, there are significant differences in the details. Note that the momentum balance estimate $\bar{\Psi}^*_m$ is notably similar among the three reanalyses. For the other two estimates, in general, the larger differences are found with MERRA, while EI and JRA-55 are more similar to each other. For instance, $\bar{\Psi}^*$ from MERRA presents a peculiar region of negative values in the lower stratosphere just north of the equator. Also, the thermodynamic estimate for MERRA shows a different structure than the rest of the estimates at ~100 hPa, with near-zero meridional velocity just above the tropical tropopause.

In order to compare the climatological structure for the different estimates more accurately, Figure 3 shows the latitudinal structure of the vertical component of the BDC for the nine estimates at four pressure levels spanning the lower and middle stratosphere. We have not interpolated the vertical velocity fields in altitude to

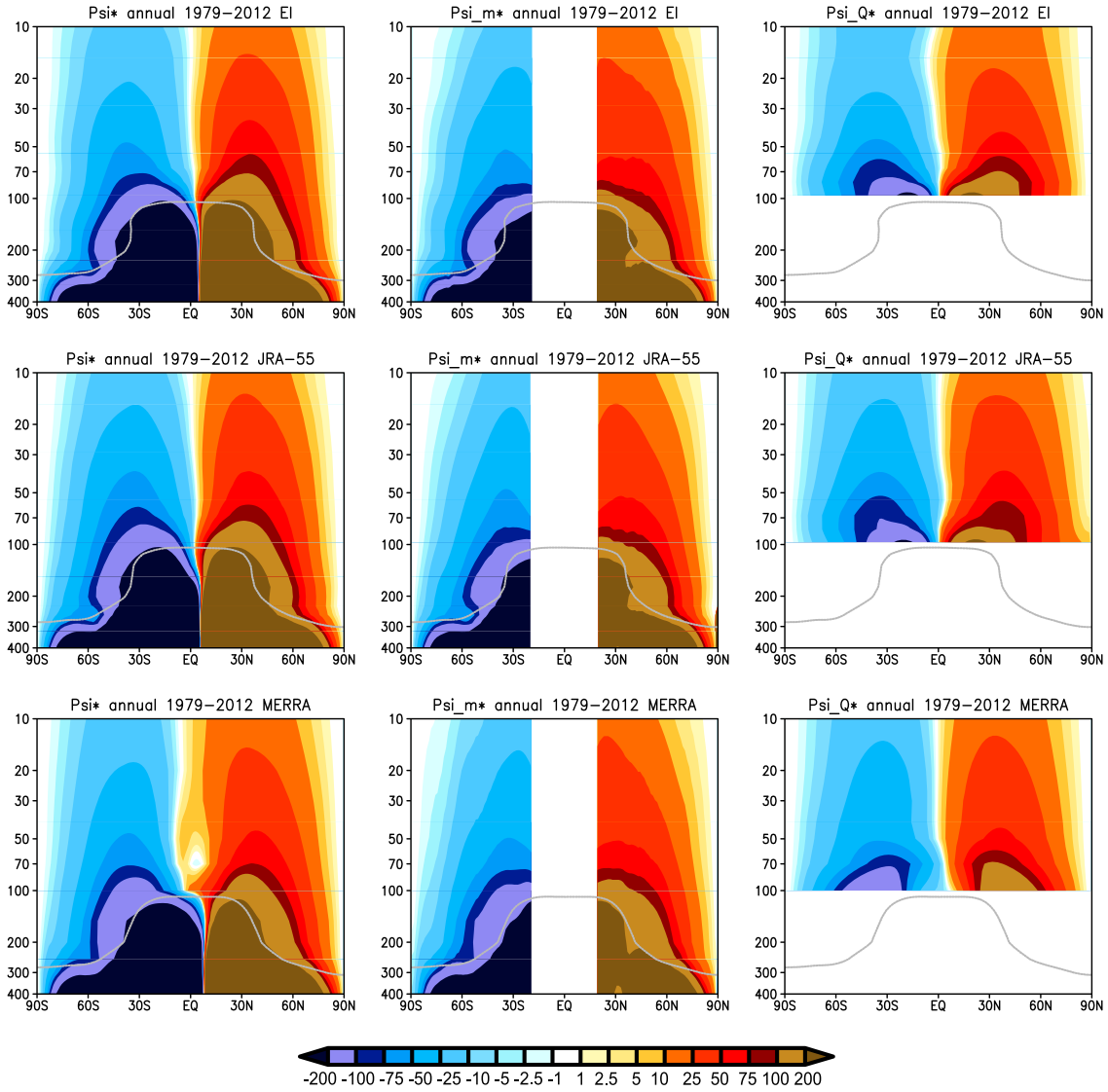

Figure 2. Latitude-height cross section of the annual mean (1979–2012) BDC stream function for the three estimates (in columns) in each of the three reanalyses (in rows). Unit: kg m^{-1} s^{-1}.

avoid excessive smoothing, and we simply select the nearest levels for each reanalysis (19, 55, 67, and 96 hPa for EI; 19, 55, 68, and 97 hPa for JRA-55; and 20, 50, 70, and 100 hPa for MERRA). Because the latitudinal structure of $\bar{w}^*_m$ cannot be computed in the deep tropics, Figure 3 shows tropical mean upwelling for the band 18°S–18°N. The overall latitudinal structure is similar in all estimates, consistent with Figure 2 (upwelling in the tropics and downwelling at high latitudes), but there are noteworthy differences. First, the momentum balance estimates present weaker downwelling over high latitudes (poleward of ~60°) than the other two estimates in all reanalyses, especially at higher levels. In addition, $\bar{w}^*_m$ shows weaker upwelling in the subtropics as compared to the other estimates. One outstanding feature is the downwelling at the equator observed only in MERRA $\bar{w}^*$ in the lower stratosphere (70 and 50 hPa), which is linked to the negative cell in the stream function highlighted in Figure 2. Finally, near the tropopause (100 hPa) the thermodynamic estimate $\bar{w}^*_Q$ is different in MERRA as compared to the other two reanalyses, which present a narrower region of tropical upwelling (in agreement with other estimates). Note that, in general, the differences are larger among the three estimates in each reanalysis than among the three reanalyses for each estimate. This is particularly clear for the momentum balance estimates, which are very similar in all reanalyses.

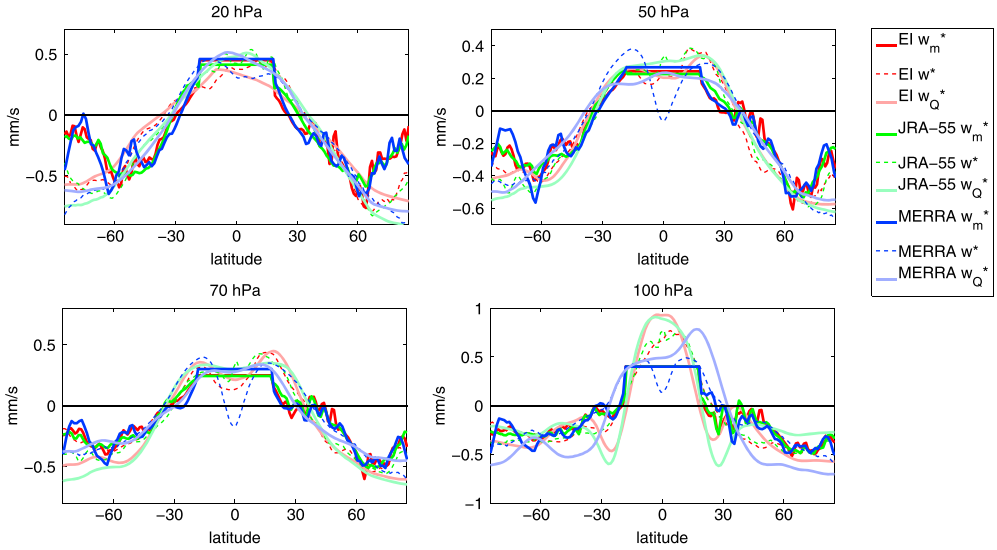

Figure 3. Latitudinal structure of the vertical component of the advective BDC on pressure levels near 20, 50, 70, and 100 hPa for the three estimates ($\bar{w}^*$, $\bar{w}^*_m$, and $\bar{w}^*_Q$) in each of the three reanalyses (EI, JRA-55, and MERRA).

3.1. Effect of the Gravity Wave Drag

As mentioned in section 2, we have evaluated the effect of the parameterized gravity waves on the momentum balance estimates ($\bar{w}^*_m$) for the three reanalyses. The magnitude of the GWD (not shown) is, in general, substantially smaller than that of the resolved wave drag (EP flux convergence) in the lower and middle stratosphere, while it is the dominant forcing in the mesosphere (above ~1 hPa). In the stratosphere, the GWD is not negligible between 10 and 1 hPa in the extratropics and in the lower stratosphere subtropics (~50% of the resolved forcing). There is an overall agreement among the reanalyses in the GWD magnitude and seasonality up to ~10 hPa, with largest GWD just above the NH subtropical jet (over the region of strongest orographic forcing) peaking in boreal winter. At higher levels all reanalyses show the largest negative GWD in the winter hemisphere extratropics. In contrast, in the summer hemisphere there are substantial discrepancies among the reanalyses, likely due to differences in the parameterizations. Particularly relevant is a strong positive (westward) GWD in the summer hemisphere extending from the mesosphere into the stratosphere (down to 10 hPa) in JRA-55. A similar summer forcing is observed only in the mesosphere (above 1 hPa) in MERRA, while negative forcing is observed below at high latitudes. In EI this summer drag is not observed at all, possibly due to the absence of nonorographic gravity wave parameterization in this reanalysis [*Seviour et al.*, 2011]. We note that the GWD is significantly smaller in EI than in the other two reanalyses, especially at high levels.

Since the forcing is weighted by density in equation (6), the large differences in the GWD at high levels do not lead to excessively large differences in the BDC below 10 hPa. Figure 4 shows the latitudinal structure of the vertical velocity estimated from momentum balance with and without the GWD contribution for the three reanalyses. The results show overall similar structures, and the main effect of the GWD is to strengthen the upwelling in the subtropics and the downwelling over polar latitudes (hence accelerating the BDC, as expected from adding more drag). The effect on the polar latitudes increases with height and it is largest for MERRA (perhaps linked to the higher top in this reanalysis), while the change in the subtropics is most evident in JRA-55. Note that a fraction of the strengthening of upwelling in the subtropics in JRA-55 is linked to the strong positive GWD in the summer hemisphere discussed above (not shown). The weakest effects are observed in EI, which presents the smallest GWD. Given the strong similarity between $\bar{w}^*_m$ and $\bar{w}^*_m$ GWD seen in Figure 4 and for the sake of a simpler interpretation, in all the following Figures the results are shown only for the resolved wave drag momentum balance estimate ($\bar{w}^*_m$). Nevertheless, the effects of including the GWD will be discussed throughout the manuscript when relevant.

3.2. Tropical Upwelling

Tropical mean upwelling is often used as a measure of the advective BDC strength, and it is computed as a surface average either averaging over a fixed latitudinal band or averaging over the turnaround (TA)

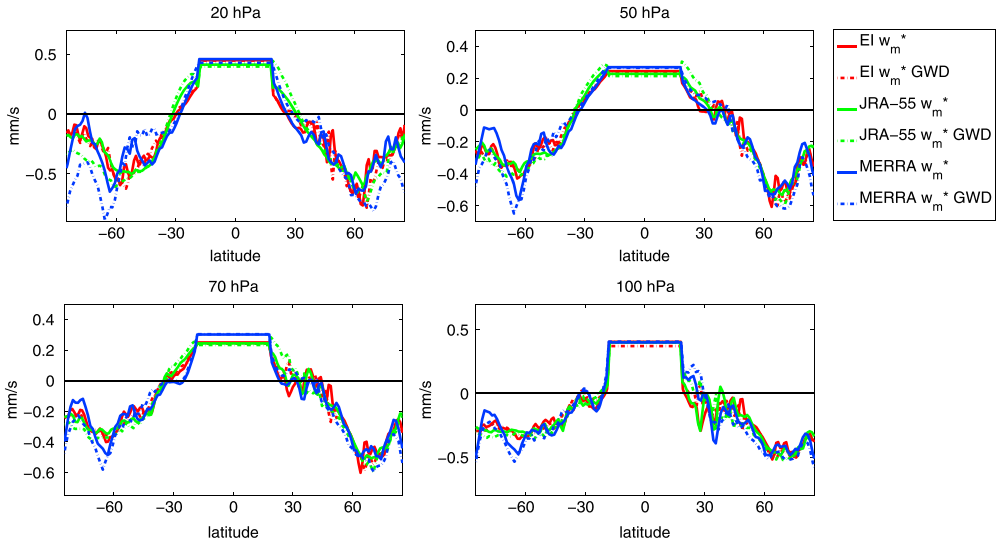

Figure 4. Effect of including the gravity wave drag (GWD) in the momentum balance calculations. Latitudinal structure of the vertical component of the advective BDC on pressure levels near 20, 50, 70, and 100 hPa for the momentum balance estimates ($\bar{w}^*_m$) computed with and without including the GWD in each of the three reanalyses (EI, JRA-55, and MERRA).

latitudes. In the present work we show results for both approaches, using 30°S–30°N as the fixed latitudinal band. The TA latitudes are defined as the boundary latitude between the region of tropical upwelling and extratropical downwelling for each month and pressure level and are computed for each reanalysis from the residual vertical velocity ($\bar{w}^*$).

Figure 5 shows the computed annual mean TA latitudes for the three reanalyses as a function of altitude, as well as the seasonality observed in the three reanalyses at 70 hPa, which is characterized by a shift in the region of upwelling toward the summer hemisphere. A similar seasonality is observed in the entire layer 100 - 10 hPa (not shown). Figure 5 shows a wider tropical upwelling region in MERRA as compared to the other two reanalyses throughout the layer, with a larger difference below 70 hPa, especially in the summer hemisphere. For EI and JRA-55, Figure 5 shows that the 30°S–30°N latitudinal band includes a region of downwelling below 70 hPa, such that the results at these lower levels averaged over fixed latitudes should be considered with caution. We have nevertheless chosen this band rather than a narrower one to encompass most of the upwelling region at all levels and thus make the results more comparable to TA latitudes.

The vertical structure of the climatological (1979–2012) annual mean tropical upwelling for each of the nine estimates is shown in Figure 6. All the estimates show an overall consistent vertical structure, with an

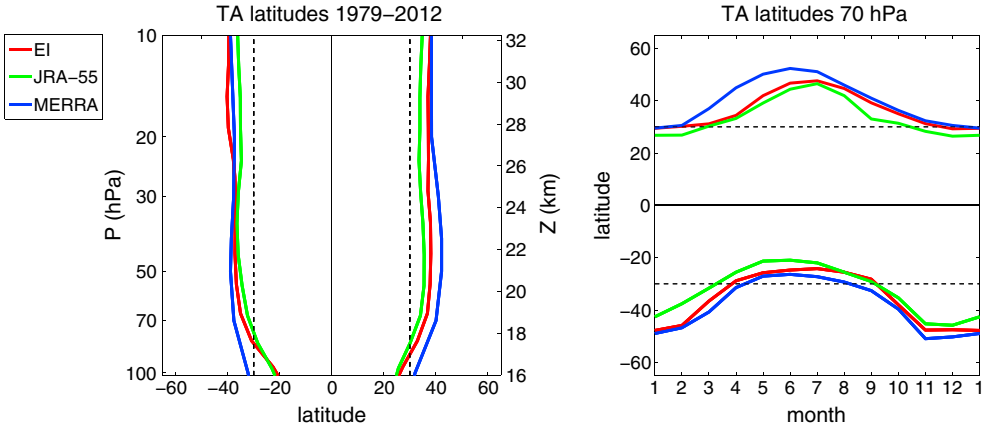

Figure 5. Turnaround (TA) latitudes in EI, JRA-55, and MERRA (left) for the annual mean as a function of altitude and (right) mean annual cycle near 70 hPa. The 30°S–30°N latitude band is shown as a dashed black line for comparison.

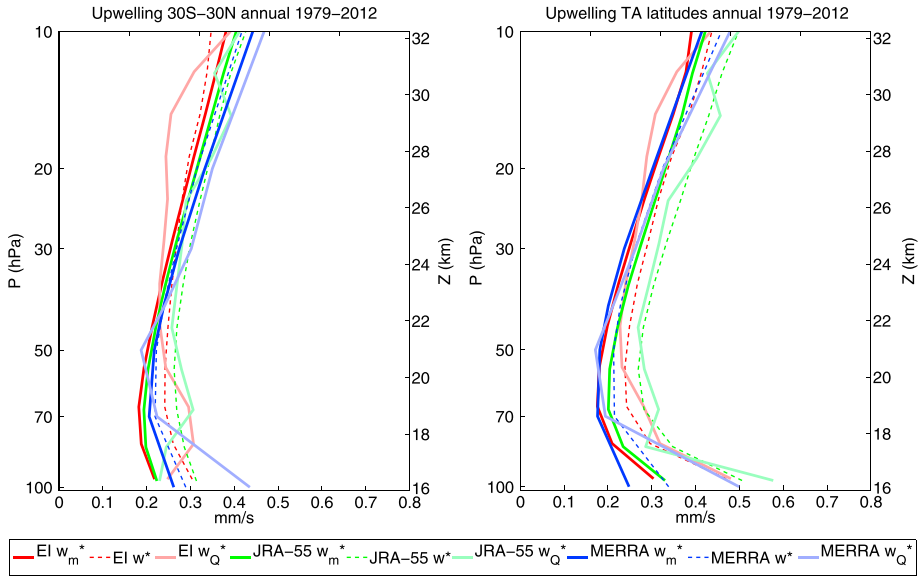

Figure 6. Annual mean tropical upwelling averaged (left) over a the 30°S–30°N latitudinal band and (right) over TA latitudes for the three estimates ($\bar{w}^*$, $\bar{w}^*_m$, and $\bar{w}^*_Q$) in each of the three reanalyses (EI, JRA-55, and MERRA). Pressure levels are shown on the left and corresponding log-pressure altitudes on the right. Average for 1979–2012.

upwelling minimum of magnitude between 0.2 and 0.3 mm s^{-1} located around 18–20 km, in agreement with previous estimates derived from satellite tracer measurements [e.g., *Schoeberl et al.*, 2008] and with free-running CCM results [e.g., *Randel et al.*, 2008]. There is significant uncertainty, given by the spread among the estimates, in the annual mean magnitude of upwelling (around 40% in the layer 70–10 hPa, and even larger below). Including the GWD in the momentum balance calculations leads to a small increase in the mean upwelling at all levels (up to 10%), which is largest for JRA-55 (not shown). The mean upwelling differs slightly between averaging over fixed and TA latitudes, with an overall larger spread among the estimates for the TA latitudes. Hence, taking into account the different TA latitudes does not improve the agreement among the reanalyses on the net upward mass flux. This could result from larger upwelling uncertainties in the region poleward of 30° (see Figures 3 and 5). Note that the band 30°S–30°N does not correspond well to the region of upwelling, especially during the solstice seasons (Figure 5). In particular, the band 30°S–30°N does not cover the entire area of upwelling above 70 hPa, and thus the upwelling values are higher for the TA latitudes than for the fixed latitudes averaging. On the other hand, below 70 hPa the range 30°S–30°N comprises relatively large downwelling regions at these levels for EI and JRA-55 (see Figure 5).

4. Tropical Upwelling Variability

The dominant feature in the time series of tropical upwelling is the annual cycle. Figure 7 shows the mean annual cycle for the 34 years period for the nine estimates of tropical upwelling in the lower stratosphere (near 70 hPa). There is a visible difference in the annual cycle amplitude between the upwelling averaged over fixed latitudes versus that averaged over TA latitudes. In particular, the annual cycle amplitude at this level is reduced from ~50% for upwelling averaged over fixed latitudes to ~25% for TA latitudes in all estimates. This implies that including the strong upwelling in the summer subtropics reduces the seasonality of the net upwelling mass flux into the stratosphere to half of that in the upwelling averaged over fixed latitudes. The reduced amplitude of the seasonality for TA latitudes as compared to fixed latitudes is a consistent feature observed throughout the layer 100–10 hPa (not shown). In Figure 7 the largest amplitudes are observed for the thermodynamic estimates ($\bar{w}^*_Q$), and the smallest for the momentum estimates ($\bar{w}^*_m$) in all reanalyses for both averaging bands. We note that including the GWD slightly increases the seasonal cycle amplitude due to larger $\bar{w}^*_m$ GWD in boreal winter, especially in EI and MERRA (not shown).

The deseasonalized upwelling monthly time series have been obtained by removing the monthly mean value for the entire period. Figure 8 shows the resulting time series of the nine deseasonalized upwelling estimates at 70 hPa, and Table 1 shows the linear correlations between them. The upwelling estimates show a high

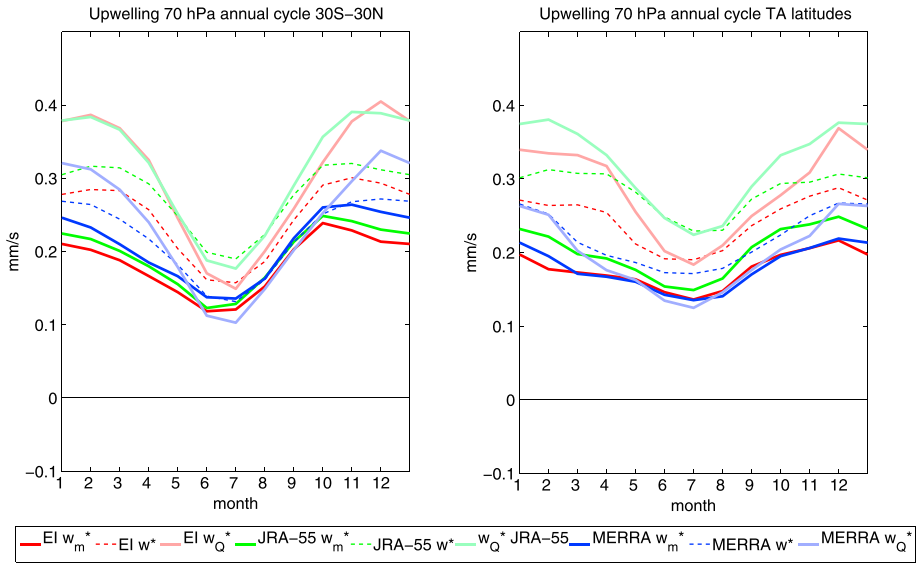

Figure 7. Annual cycle of tropical upwelling near 70 hPa for (left) fixed latitudes and (right) turnaround latitudes for the three estimates ($\bar{w}^*$, $\bar{w}^*_m$, and $\bar{w}^*_Q$) in each of the three reanalyses (EI, JRA-55, and MERRA). Average for 1979–2012.

degree of common variability from month-to-month to interannual timescales, with overall similar behavior between TA and fixed latitudes averaging. The linear correlations between all pairs of tropical upwelling time series are statistically significant at the 99% confidence level at 70 hPa using a two-tailed Student's *t* test (Table 1). The lowest correlations are found between the thermodynamic balance estimates ($\bar{w}^*_Q$) and the other two estimates, probably linked to the large uncertainties in the heating rates in the lower tropical stratosphere (discussed in *Wright and Fueglistaler* [2013]). The highest correlations (>0.9 for fixed latitudes averaging) are found between the momentum balance estimates ($\bar{w}^*_m$), reflecting the strong similarity between the resolved EP fluxes in the different reanalyses. Including the GWD has a small impact on the variability, and the correlations of $\bar{w}^*_m$ *GWD* with the other estimates are very similar to those shown in Table 1 (not shown). Only for JRA-55 the correlations decrease slightly when including the GWD, likely due to the effect of the strong GWD in the summer upper stratosphere in this reanalysis. In Table 1 the correlations between the different reanalyses

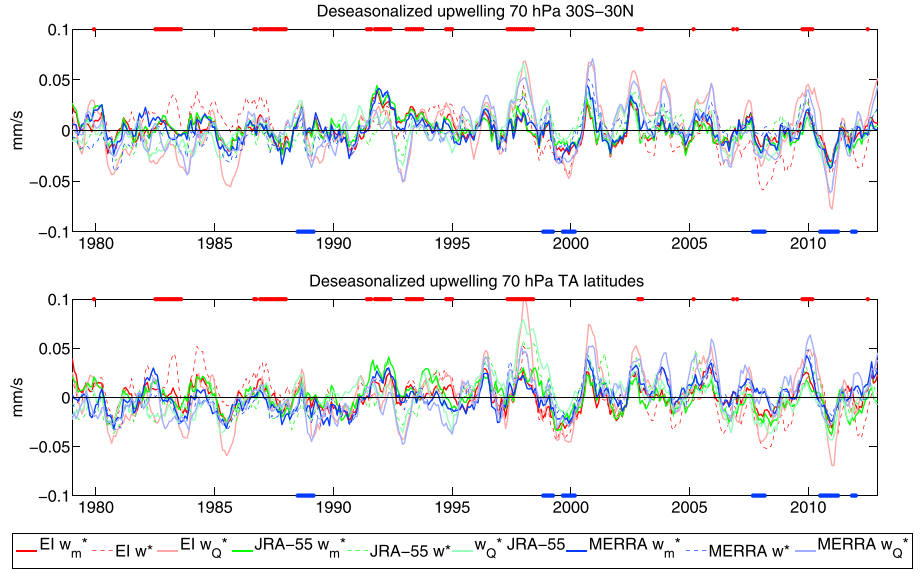

Figure 8. Time series of deseasonalized upwelling near 70 hPa averaged over (top) fixed latitudes and (bottom) turnaround latitudes for the three estimates ($\bar{w}^*$, $\bar{w}^*_m$, and $\bar{w}^*_Q$) in each of the three reanalyses (EI, JRA-55, and MERRA). The red and blue dots indicate major positive (El Niño) and negative (La Niña) events, respectively (see text for details).

Table 1. Linear Correlations Between the Time Series of Tropical Upwelling at 70 hPa Shown in Figure 8 for the Case of Averaging Between Fixed Latitudes (30°S–30°N, Above) and TA Latitudes (Below)[a]

	$\bar{w}^*$ EI	$\bar{w}^*$ JR	$\bar{w}^*$ ME	$\bar{w}^*_m$ EI	$\bar{w}^*_m$ JR	$\bar{w}^*_m$ ME	$\bar{w}^*_Q$ EI	$\bar{w}^*_Q$ JR	$\bar{w}^*_Q$ ME
30°S–30°N									
$\bar{w}^*$ EI	1.00	0.60	0.64	0.70	0.72	0.67	0.41	0.41	0.46
$\bar{w}^*$ JR	–	1.00	0.88	0.74	0.73	0.74	0.60	0.61	0.55
$\bar{w}^*$ ME	–	–	1.00	0.82	0.81	0.82	0.63	0.64	0.63
$\bar{w}^*_m$ EI	–	–	–	1.00	0.94	0.91	0.44	0.48	0.42
$\bar{w}^*_m$ JR	–	–	–	–	1.00	0.91	0.42	0.50	0.41
$\bar{w}^*_m$ ME	–	–	–	–	–	1.00	0.46	0.50	0.47
$\bar{w}^*_Q$ EI	–	–	–	–	–	–	1.00	0.74	0.85
$\bar{w}^*_Q$ JR	–	–	–	–	–	–	–	1.00	0.79
$\bar{w}^*_Q$ ME	–	–	–	–	–	–	–	–	1.00
TA latitudes									
$\bar{w}^*$ EI	1.00	0.45	0.47	0.77	0.60	0.50	0.57	0.34	0.27
$\bar{w}^*$ JR	–	1.00	0.64	0.52	0.73	0.60	0.51	0.68	0.46
$\bar{w}^*$ ME	–	–	1.00	0.63	0.62	0.87	0.47	0.46	0.70
$\bar{w}^*_m$ EI	–	–	–	1.00	0.71	0.73	0.55	0.33	0.33
$\bar{w}^*_m$ JR	–	–	–	–	1.00	0.69	0.38	0.58	0.32
$\bar{w}^*_m$ ME	–	–	–	–	–	1.00	0.43	0.40	0.60
$\bar{w}^*_Q$ EI	–	–	–	–	–	–	1.00	0.62	0.66
$\bar{w}^*_Q$ JR	–	–	–	–	–	–	–	1.00	0.57
$\bar{w}^*_Q$ ME	–	–	–	–	–	–	–	–	1.00

[a] All correlations are statistically significant at the 99% confidence level using a two-tailed t-Student test.

(for a given estimate) are higher for the average over fixed latitudes than over TA latitudes, likely due to the weaker consistency among the reanalyses in the variability of the TA latitudes than in other quantities (e.g., temperature, zonal wind, and EP flux). Nevertheless, in general, the agreement between different estimates in each reanalysis is improved using TA as compared to fixed latitudes (see Table 1). Similar results apply throughout the altitude range considered (100–10 hPa), with statistically significant correlations between all the upwelling estimates. The only exceptions are found near the tropopause. In particular, at ~100 hPa none of the estimates correlate with $\bar{w}^*_Q$ computed from EI and JRA-55 averaged over fixed latitudes. This is likely because these two estimates include regions of strong downwelling within the averaging latitudes of 30°S–30°N (see Figure 3).

4.1. Influence of the QBO and ENSO

The time series of the upwelling estimates in the lower stratosphere in Figure 8 show a number of consistent peaks related to major ENSO events, with positive (negative) ENSO index linked to enhanced (reduced) upwelling in the tropical lower stratosphere, in agreement with previous studies [e.g., *Calvo et al.*, 2010]. A QBO modulation is also observed in the time series, mostly at higher levels, with stronger (weaker) tropical mean upwelling during the easterly (westerly) shear phase, as expected [e.g., *Baldwin et al.*, 2001]. In order to quantify the influence of the QBO and ENSO in the upwelling estimates, we performed a multiple-regression analysis. For the QBO we use two indices corresponding to the first two empirical orthogonal functions (EOFs) of the zonal wind around the equator (here ~5°S–N) over the layer 70–10 hPa for each reanalysis (following *Wallace et al.* [1993]). For ENSO, we use the monthly multivariate ENSO index from NOAA [*Wolter and Timlin*, 1998]. Figure 9 shows the fraction of variance in deseasonalized upwelling associated with ENSO and with the QBO as a function of altitude. There is a large spread among the estimates, but some common general aspects are observed. In particular, the fraction of variance associated with the QBO increases with height up to ~20 hPa and then decreases above for all estimates, while the ENSO variability peaks in the lower stratosphere and rapidly decreases above and below. The QBO variance increases more sharply for the TA-averaged upwelling than for the fixed latitudes, reaching up to 45% near 20 hPa. Hence, a larger fraction of the QBO

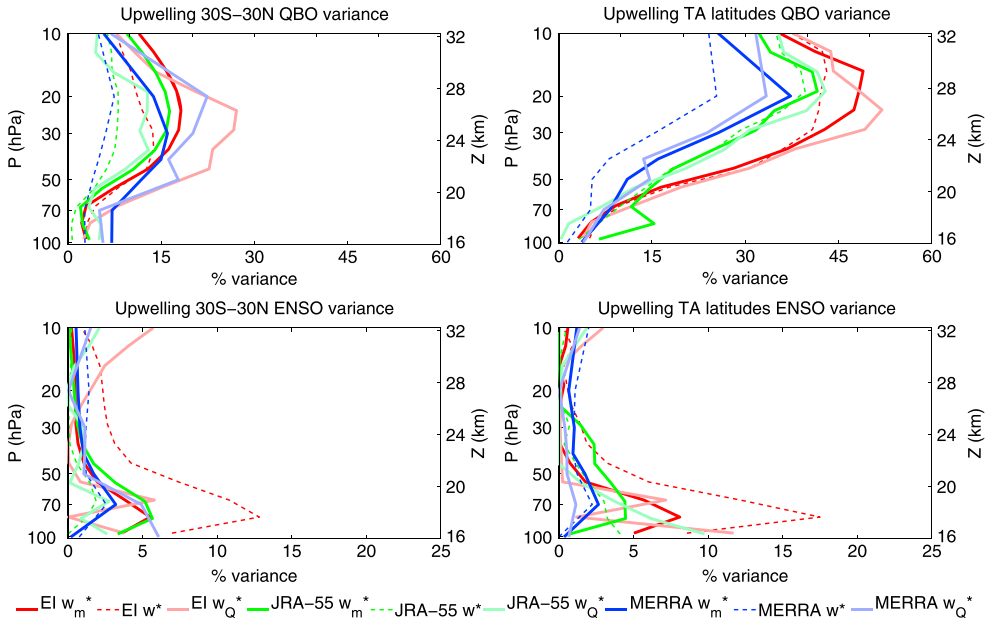

Figure 9. Fraction of variance in deseasonalized tropical upwelling associated with the QBO and ENSO (obtained by multiple linear regression, see text for details) as a function of altitude. The results are shown for upwelling averaged over (left) fixed latitudes and (right) turnaround latitudes. Pressure levels are shown on the left and corresponding log-pressure altitudes on the right.

variability is captured when averaging upwelling between the TA latitudes as compared to fixed latitudes. This is consistent with a significant QBO-related variability of the TA latitudes in the three reanalyses (not shown). The ENSO-related variance in tropical upwelling peaks around 80–70 hPa in all estimates and explains less than 10% of the variance. The residual circulation for EI has larger variance associated with ENSO (slightly above 15%). Note that there could be an overlap between the QBO and ENSO signals at 70 hPa and below [*Davis et al.*, 2013]. Although not shown here, we note that the latitudinal structure of the variance associated with the QBO shows a strong peak around the equator, which explains up to ∼90% of the variability near 20 hPa (plus two secondary peaks around ∼20°S and ∼20°N). The ENSO component is more uniformly distributed over the tropics. We note that these results are qualitatively consistent with the QBO and ENSO variance in the AoA computed from the EI reanalysis in *Diallo et al.* [2012].

4.2. Links to the Stratospheric Sudden Warmings and Volcanic Eruptions

Figure 10 shows the deseasonalized upwelling time series at 70 hPa after removing (from the series in Figure 8) the QBO and ENSO variability obtained by multiple linear regression. The upwelling series still present a high degree of common variability, with several fluctuations observed consistently in most estimates (the statistically significant linear correlations are slightly smaller than those in Table 1). In particular, all estimates show a number of peaks of strong upwelling after the year 1998, coinciding with an increased frequency of stratospheric sudden warming (SSW) events in this period as compared to the previous decade. The major SSW events are shown in Figure 10, computed following *Charlton and Polvani* [2007] from EI data (the results for the other two reanalyses are similar), plus the event observed in the SH in September 2002. Several of these events are observed coherently with strong positive anomalies in the upwelling estimates at 70 hPa. Nevertheless, other strong upwelling events occur without correspondence to a major SSW, as it is the case of the late year 2000, which was associated with a strong anomaly in SH eddy heat flux, as reported in *Fueglistaler et al.* [2014].

Figure 10 also includes two major volcanic eruptions (El Chichón, April 1982, and Pinatubo, June 1991). After the Pinatubo eruption a weakened upwelling is clearly observed only in the thermodynamic estimates, while some of the other estimates show the opposite behavior. In particular, all momentum balance estimates ($\bar{w}^*_m$) show a strengthening of the circulation after the Pinatubo eruption. This difference between the dynamical and thermodynamical upwelling estimates is less pronounced after the El Chichón eruption, although it remains unclear if this reflects a different dynamical response for both eruptions (as proposed by

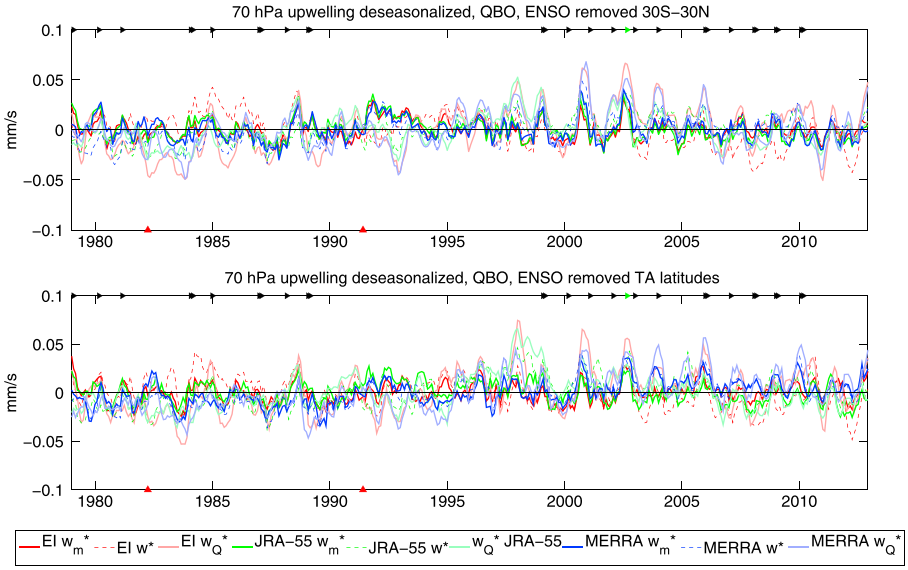

Figure 10. Time series of deseasonalized upwelling near 70 hPa averaged over (left) fixed latitudes and (right) turnaround latitudes after removing the variability associated with QBO and ENSO. A five-point running mean has been applied to the monthly time series. Black triangles show the major SSW (in green the SH event in September 2002), and red triangles at the bottom correspond to the El Chichón (approximately April 1982) and Pinatubo eruptions (June 1991).

Fueglistaler et al. [2014]). A crucial point is that none of the reanalyses assimilate aerosol data in the radiative scheme, and thus the heating rates do not know about the strong aerosol loading associated with the volcanic emissions [e.g., *Simmons et al.*, 2014]. The reanalyses' tropical mean heating rates consistently show a strong negative anomaly just after the eruption at ~30 hPa (~25 km, the altitude of the aerosol cloud [e.g., *McCormick and Veiga*, 1992]), which descends toward the lower stratosphere in a timescale of more than 1 year (see Figure 1). The diabatic cooling anomaly is likely induced in the reanalyses' radiative models to compensate the increase in (observed) temperature and leads to corresponding negative anomalies in upwelling from thermodynamic balance ($\bar{w}^*_Q$). Note that, despite the removal of the QBO and ENSO signals, some residual influence of this variability remains, due to possible nonlinear interactions between them or with other processes (for example, the 1997/1998 strong ENSO event is visible in the TA latitudes thermodynamic estimates in Figure 10). In particular, the interference with ENSO and QBO signals could lead to differences in the dynamical responses to the volcanic eruptions [e.g., *Graf et al.*, 2007].

5. Trends

5.1. Trends in Tropical Upwelling

Figure 11 shows the 1979–2012 trends in annual mean tropical upwelling as a function of altitude in the layer 100–10 hPa. The trends are computed by simple least squares regression after removing the ENSO and QBO variability from the deseasonalized upwelling time series (cf. Figure 10), and their statistical significance is determined for the 95% confidence level using a bootstrap resampling technique [e.g., *von Storch and Zwiers*, 1999]. We note that the trends are practically unchanged when the variance linked to ENSO and the QBO is not removed. There is significant spread among the estimates and the results differ quantitatively between the fixed latitudes and the TA latitudes averaging. Nevertheless, most estimates consistently show a positive trend in tropical upwelling throughout the lower and middle stratosphere. Only the residual circulation ($\bar{w}^*$) from EI persistently shows negative trends for both averaging bands over most of the layer 100–10 hPa, consistently with the results of *Seviour et al.* [2011] for the lower stratosphere. The largest spread in the trends is found at lower levels (in particular MERRA shows larger values of 4–8%/decade for TA latitudes at 100 and 70 hPa). On the other hand, above ~23 km several estimates show trends between 2 and 4%/decade. We have tested that the trends are very similar when the years after the main volcanic eruptions are removed (not shown). Note that the momentum balance estimates, in general, give smaller and often nonsignificant trends (except for MERRA averaged over TA latitudes at lower levels). Introducing the GWD in the momentum balance estimates does not significantly change the trends, consistently with the obtained negligible changes in the overall variability.

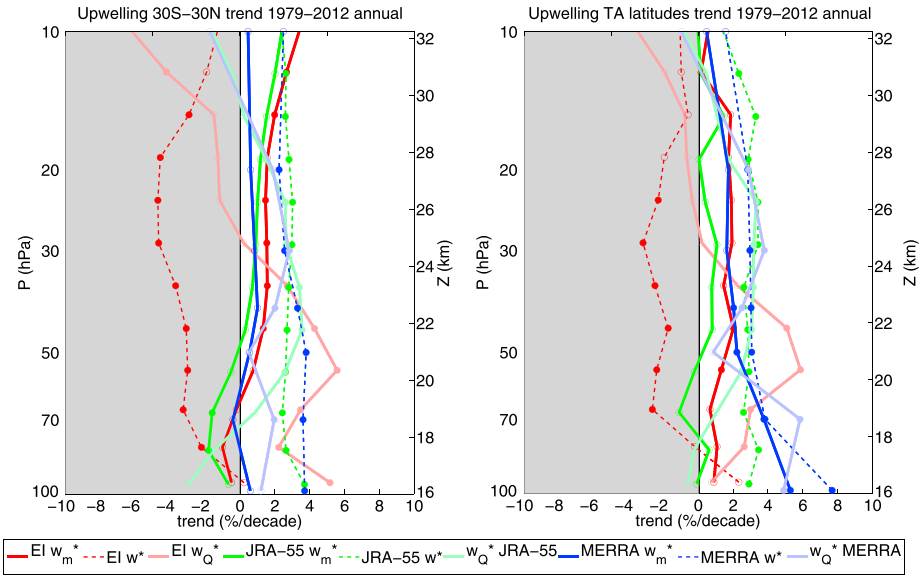

Figure 11. Linear trends in annual mean tropical upwelling for 1979–2012 as a function of altitude: (left) 30°S–30°N and (right) TA latitudes. The time series are previously deseasonalized and the QBO and ENSO variability is removed by linear regression (as in Figure 10). Statistically significant trends at the 95% level are indicated by filled circles. The black line indicates the zero trend line and the gray shading highlights the region of negative trends. Pressure levels are shown on the left and corresponding log-pressure altitudes on the right.

Figure 12 shows the statistically significant trends in upwelling averaged over TA latitudes for the four seasons of the period 1979–2012 (the results for 30°S–30°N averaging are not shown for simplicity, but they are qualitatively similar). In all seasons the trends are predominantly positive, with negative values mainly corresponding to the EI $\bar{w}^*$ estimate (as seen for the annual mean in Figure 11). The most coherent positive trends are found in September–November (SON), where almost all estimates show significant strengthening of tropical upwelling (between 2 and 6%/decade) throughout the lower and middle stratosphere. Inspection of the SON time series (not shown) highlights persistently increasing upwelling mainly over the period 1979–2002, culminating with large upwelling positive anomalies in 2000 and 2002 (corresponding with years of strongly

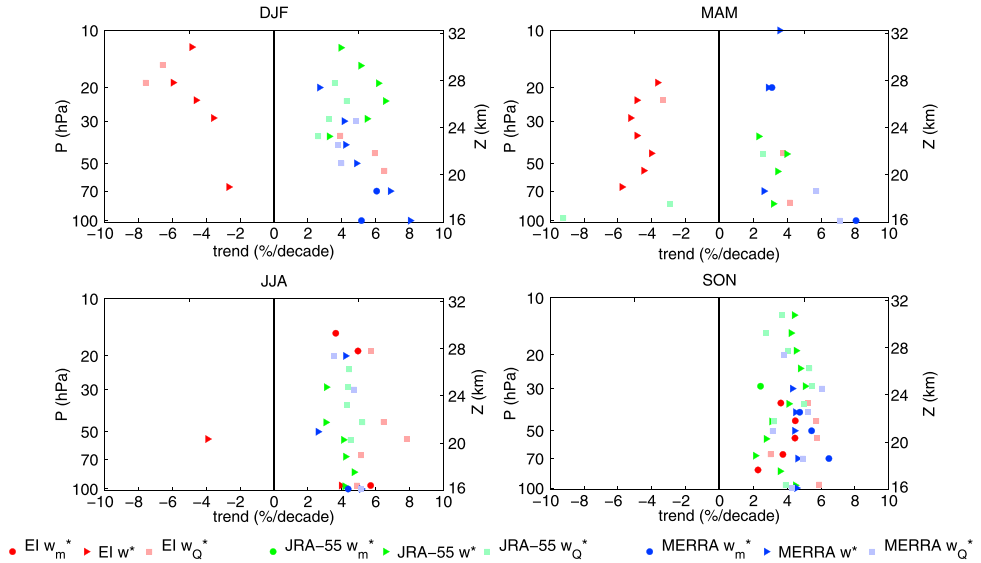

Figure 12. Linear trends in tropical upwelling averaged over TA latitudes as a function of altitude for DJF, MAM, JJA, and SON. The time series are previously deseasonalized and the QBO and ENSO variability is removed by linear regression. Only statistically significant trends at the 95% level are shown.

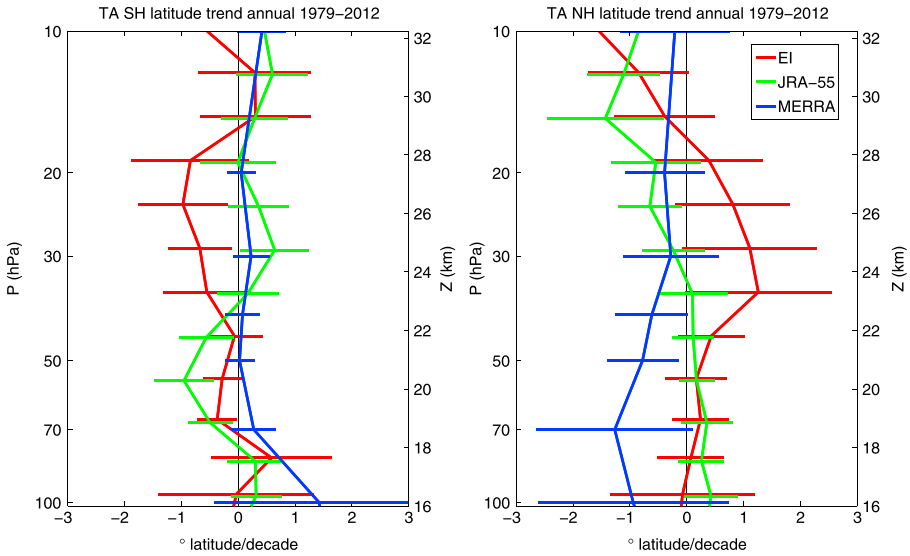

Figure 13. Linear trends for 1979–2012 in the annual mean turnaround latitudes for EI, JRA-55, and MERRA as a function of altitude. Error bars are computed using the 95% statistical significance level with the corresponding degrees of freedom accounting for the autocorrelation in the series. Pressure levels are shown on the left and corresponding log-pressure altitudes on the right.

perturbed SH vortex). The least consistent trends in Figure 12 are found in March–May (MAM), where only a few estimates show significant trends. Trends in December–February (DJF) and June–August (JJA) are mainly positive throughout the altitude range, although there are fewer statistically significant estimates at each level than for SON. Note that the negative trends in EI $\bar{w}^*$ (and $\bar{w}^*_Q$ at upper levels) in Figure 11 are mainly linked to DJF and MAM.

Some of the differences between the fixed latitudes and the TA latitudes upwelling trends seen in Figure 11 can be explained by long-term changes in the position of the TA latitudes. Figure 13 shows the trends in the annual mean TA latitudes for the three reanalyses. Remarkably, each reanalysis shows different behavior and no consistent trend can be extracted for the width of the tropical upwelling region. The narrowing of the tropics in MERRA is responsible for the large difference between Figure 11 (left) and Figure 11 (right) at 70 and 100 hPa, since in the last decade the 30°S–30°N band includes a region of downwelling which partly compensates the increase in upwelling at lower latitudes (especially in the NH tropics). On the other hand, the positive trend in NH TA latitude around 50–20 hPa for EI is mainly linked to significant poleward displacement in JJA (with trends up to $\sim 3.5 \pm 1.5$°/decade). This widening leads to smaller negative trends in $\bar{w}^*$ for TA latitudes as compared to fixed latitudes averaging in Figure 11. We note that these trends, observed only in one reanalysis, could result from artificial discontinuities in the data. Overall, Figure 13 highlights substantial differences and thus large uncertainties in the temporal evolution of the TA latitudes among reanalyses.

5.2. Trends in the Global BDC

In order to have a comprehensive perspective of the changes in the circulation independently of the averaging latitudes, we examine the global structure of the advective BDC trends. The annual mean trends of the BDC stream function as a function of latitude and altitude for the nine estimates are shown in Figure 14 (similar to Figure 2 for the climatology). There is a wide spread in the results, with apparent differences in the spatial structure of the trends. An outstanding feature is the counterclockwise circulation cell in the NH subtropics above 70 hPa in the residual circulation stream function ($\bar{\Psi}^*$) computed from EI (first panel in Figure 14, with implied downwelling over the tropics. This negative trend in the BDC stream function is consistent with the weakening upwelling trend obtained for $\bar{w}^*$ from EI (Figures 11 and 12). Aside from this feature all estimates show positive trends in the NH and negative trends in the SH, indicating a strengthening of the annual mean BDC in both hemispheres. Such intensification in the global advective BDC suggested by Figure 14 is consistent with the acceleration in tropical mean upwelling throughout the layer 100–10 hPa seen in Figure 11. Although the acceleration of the circulation is a qualitatively robust result across the estimates, the details of the trend patterns differ substantially, and it is not possible to derive general conclusions regarding the trends

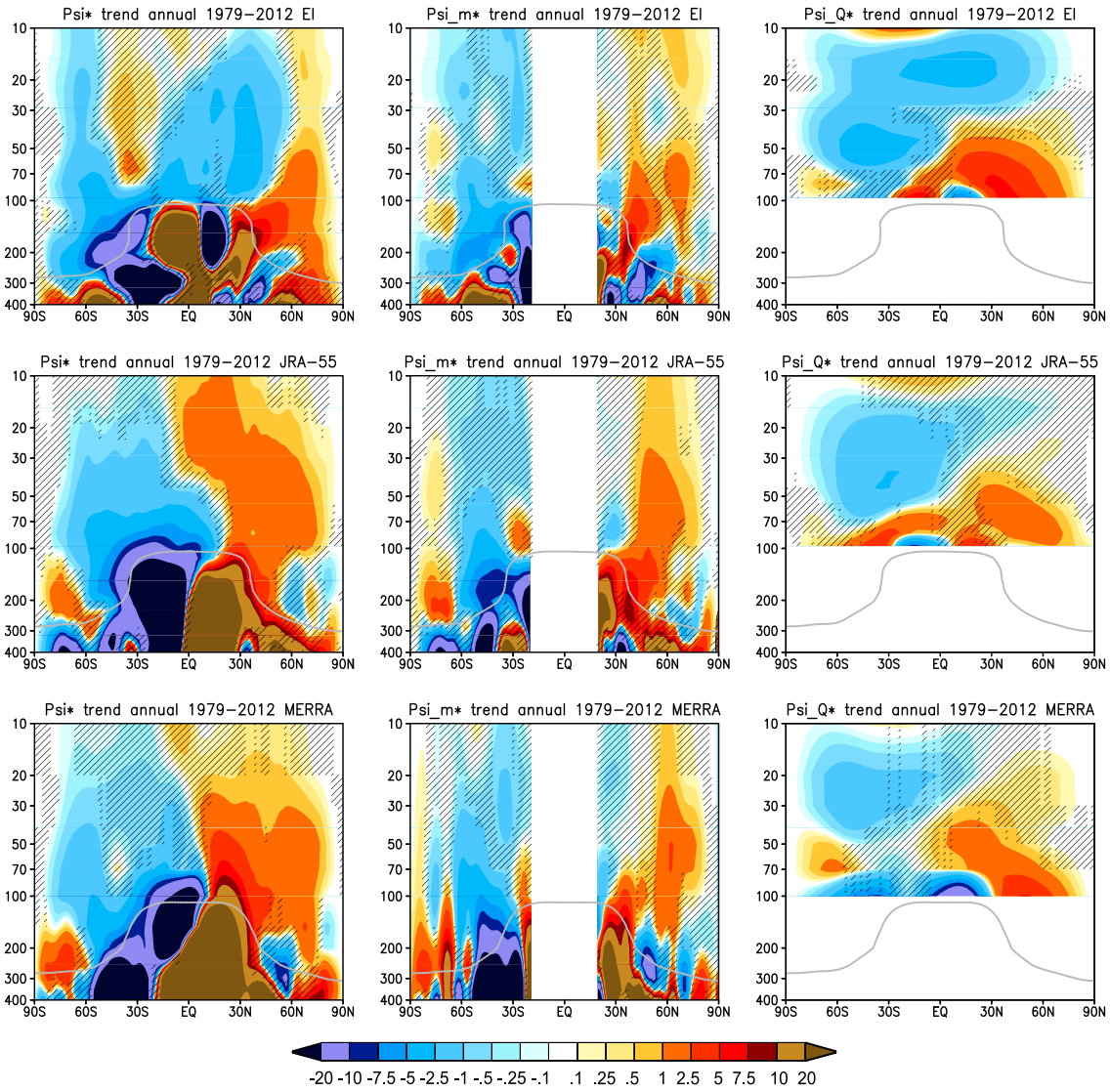

Figure 14. Annual mean linear trends (1979–2012) in the BDC stream function for the nine estimates (as in Figure 2). Unit: kg m^{-1} s^{-1} $decade^{-1}$. The regions of nonstatistically significant trends at the 95% level are hatched. The annual mean tropopause for 1979–2012 is shown by the gray line.

in the shallow versus deep branches. We note that, as found for tropical upwelling trends, including the GWD in the momentum balance estimates does not change significantly the trends in the total forcing or the BDC (not shown).

The annual mean BDC trends in Figure 14 are associated with changes in all seasons, but the coherence among the estimates and the spatial distribution of the trends varies substantially. In particular, the DJF trends make a major contribution to the overall structure of the annual mean trends and are the most coherent across the different reanalyses and estimates. Figure 15a shows the DJF trends in the momentum balance estimate $\bar{\Psi}^*_m$ averaged for the three reanalyses (the multi-reanalysis mean is very similar to any of the single reanalysis results). The DJF trends in Figure 15a present strong acceleration cells in the extratropics of both hemispheres, centered around 70 hPa and 60°S/N, similar to the behavior observed for the annual mean in Figure 14. This structure is consistently observed in all the estimates and reanalyses (not shown). We recall that the most coherent trends in tropical mean upwelling are observed in SON (Figure 12) and not in DJF as for the global BDC. This difference is probably due to the fact that the BDC trends in DJF are mainly located away from the tropics (see Figure 15a). The corresponding $\bar{\Psi}^*_m$ trends in SON are shown in Figure 15c, and they are overall smaller and less significant than those for DJF. There is also less consistency among the trends in the different estimates in SON (not shown). However, the trends are located closer to the tropical region in Figure 15c (and

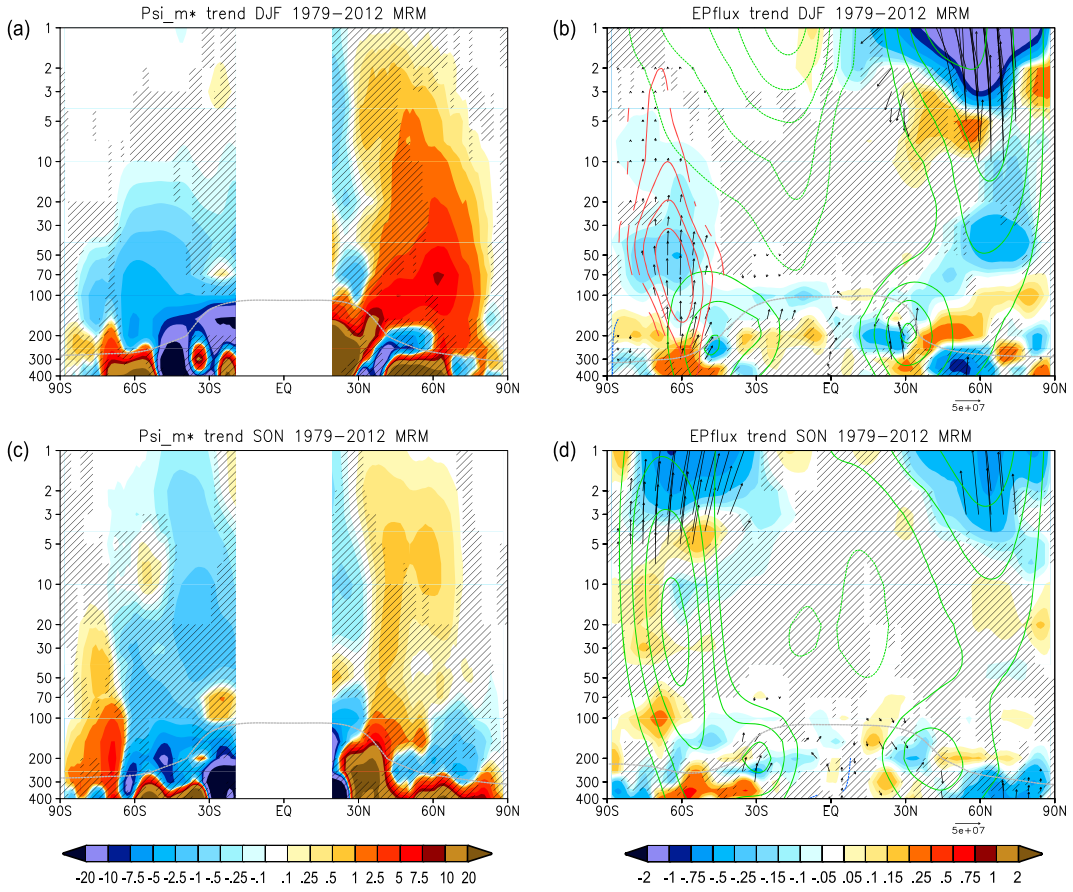

Figure 15. (a and c) Linear trends of the momentum balance stream function ($\bar{\Psi}^*_m$) for DJF (Figure 15a) and SON (Figure 15c) averaged for the three reanalyses (multi-reanalysis mean, MRM). Unit: kg m^{-1} s^{-1} decade^{-1}. (b and d) Linear trends of the EP flux (arrows) and EP flux divergence (shading, in m s^{-1} d^{-1} decade^{-1}) for DJF (Figure 15b) and SON (Figure 15d) averaged for the three reanalyses. EP fluxes are scaled by density (unit: kg s^{-2} decade^{-1}) and the vertical component is multiplied by $0.5 \cdot 10^3$. Trends in zonal mean wind are shown by the red (positive) and blue (negative) contours (contour spacing is 0.3 m s^{-1} decade^{-1}, zero contour omitted). Green contours show the seasonal mean zonal mean wind (contour spacing is 10 m s^{-1}, zero contour omitted). The regions of nonstatistically significant trends at the 95% level are hatched. The seasonal mean tropopause for 1979–2012 is shown by the gray line.

in other estimates, not shown), which might explain the coherence in tropical upwelling trends in Figure 12. Note that Figure 15 includes upper stratospheric levels up to 1 hPa and shows statistically significant strengthening of the circulation ($\bar{\Psi}^*_m$) also above 10 hPa (in both hemispheres in SON, only in the NH in DJF). However, it is important to point out that, while there is high consistency in the $\bar{\Psi}^*_m$ results for the three reanalyses, the upper level trends are less consistent in the $\bar{\Psi}^*$ estimates and are not present at all in $\bar{\Psi}^*_Q$ (which are dominated by strong artificial discontinuities in the heating rates at the upper levels, as shown in Figure 1).

Trends in the momentum balance estimate $\bar{\Psi}^*_m$ are necessarily linked to changes in the resolved wave drag, and Figures 15b and 15d show the trends in the EP fluxes and zonal winds averaged for the three reanalyses for DJF and SON, respectively. We note that the trends are remarkably consistent among the reanalyses for these two seasons (not shown). The DJF trends in the EP flux (Figure 15b) highlight two main regions of intensified wave drag below 10 hPa, one in each hemisphere. In the SH there is an enhancement of wave propagation into the stratosphere over a region of westerly acceleration centered above and poleward of the climatological subtropical jet and extending over a deep layer. These waves converge around 60°S between ~70–30 hPa, driving at least in part the BDC acceleration in the SH in this season (Figure 15a). The SH summer (DJF) trends in the zonal wind have been noted previously in both observations [e.g., *Thompson and Solomon*, 2002] and models [e.g., *Son et al.*, 2008; *McLandress et al.*, 2010] and are linked to ozone depletion in the SH lower stratosphere [*Gillett and Thompson*, 2003; *Son et al.*, 2010]. The reduced spring ozone leads to a slower warming of the SH polar lower stratosphere and thus delays the vortex breakup date, resulting in a westerly

trend in the austral summer [*Waugh et al.*, 1999; *Son et al.*, 2010]. This trend is clearly observed in the three reanalyses and is consistent with the strengthening of the meridional circulation in the SH summer. On the other hand, in the NH there is an increasing trend in EP flux convergence in the lower part of the polar vortex, coincinding with the NH acceleration cell in the lower stratosphere in Figure 15a. There is also a weakening trend in the polar vortex, although this trend in the zonal wind is not visible in Figure 15b because it is not statistically significant at the 95% level (due to the large variability in the winter hemisphere). The NH trend is mainly associated with a strengthening of the DJF circulation in the 2000's, reflected in the increased number of major SSWs since 1998 shown in Figure 10. In fact, these trends are not observed if the period after 1998 is not considered (e.g., 1979–1997, not shown). Finally, Figure 15b also shows strong trends in the EP flux convergence in the NH above 10 hPa, which are consistent with the acceleration of the BDC at these upper levels and could also contribute to the $\bar{\Psi}^*_m$ trends below 10 hPa (especially the high-latitude downwelling). The SON trends in the EP flux and zonal wind (Figure 15d) show a clear enhancement of the wave drag at high levels (above 10 hPa) in both hemispheres, which drive the upper level trends in the BDC observed in Figure 15c. We note that the trends in MAM and JJA also contribute to the annual mean trends in Figure 14, especially in the lower stratosphere, and there are corresponding trends in the EP flux convergence above the subtropical jets (not shown).

6. Summary and Discussion

In this work we examine the advective BDC in three modern reanalyses (EI, JRA-55, and MERRA) for the period 1979–2012 in the lower and middle stratosphere below 10 hPa. For each reanalysis we calculate three different diagnostics, namely the residual circulation ($\bar{v}^*$, $\bar{w}^*$) and two indirect estimates derived from momentum ($\bar{v}^*_m$, $\bar{w}^*_m$) and thermodynamic ($\bar{v}^*_Q$, $\bar{w}^*_Q$) balances in the TEM formalism. The results show a relatively large spread among the estimates (around 40%) in the magnitude of tropical upwelling, which can be due to several sources of uncertainty in the calculations, including uncertainties in the reanalysis data (e.g., in the velocity fields and the heating rates), the different assimilation increments in each reanalysis and the possible discontinuities in the assimilated data. Despite these uncertainties there is significant coherent variability among the nine BDC estimates. In addition to the dominant annual cycle all estimates show common interannual variability, with important contributions from the QBO and ENSO (Figure 9). An impact of major SSW events and volcanic emissions is also observed in the upwelling time series (Figure 10). The largest differences in the variability are found near the tropopause (~100 hPa), especially for the thermodynamic estimates (likely due to large uncertainties in the reanalyses heating rates [e.g., *Fueglistaler et al.*, 2009; *Wright and Fueglistaler*, 2013]). At higher levels all the correlations among the nine estimates of tropical upwelling are statistically significant at the 99% level, with strongest agreement among the momentum balance estimates.

The trends in tropical upwelling show significant spread but overall suggest a strengthening over the layer 100–10 hPa for the period 1979–2012 of order 2–5% per decade (Figure 11), which is approximately consistent with model results [*Lamarque and Solomon*, 2010; *Butchart et al.*, 2010]. This behavior is observed for most estimates, with the important exception of the residual circulation from EI ($\bar{w}^*$), which shows opposite trends. The weakened tropical upwelling based on EI $\bar{w}^*$ is consistent with the results of *Seviour et al.* [2011], but this particular estimate clearly appears as an outlier when put into context among the other estimates in the present work (Figure 11). Hence, these results present evidence of statistically significant acceleration of the advective BDC in the last decades from reanalysis data. The diversity of estimates highlights the large uncertainties in the results but at the same time provides robustness to the consistent features.

The latitudinal structure of the momentum balance estimate ($\bar{w}^*_m$) reveals weaker upwelling in the subtropics and downwelling at high latitudes than the other estimates (see Figure 3). Additional calculations explicitly including the gravity wave drag (GWD) provided by the reanalyses in the momentum balance estimates show a slight increase in tropical upwelling and extratropical downwelling (Figure 4). Although these changes go in the right direction, the magnitude is not enough to explain the differences with the other estimates, suggesting that other uncertainties in addition to parameterized gravity waves are important in the momentum balance calculations.

The tropical upwelling results are presented both averaged over a fixed range of latitudes (30°S–30°N) and averaged over the turnaround (TA) latitudes (position of zero upwelling lines). While the calculated TA latitudes are similar among the reanalyses in their annual mean location and seasonality, there are large differences regarding the interannual variability and long-term trends (Figure 13). The correlations between

upwelling estimates averaged over TA latitudes in different reanalyses are lower than those for fixed latitudes, which implies that taking into account the different width of the tropics does not improve the consistency among reanalyses. These results highlight the poor agreement in the representation of the TA latitudes variability in reanalyses.

The trends in the global advective BDC stream function for the period 1979–2012 show qualitative agreement among estimates (except for the EI residual circulation stream function), with statistically significant acceleration of the circulation in the extratropics of both hemispheres for the annual mean (Figure 14). These trends in the global BDC are consistent with the overall increase in upwelling shown in Figure 11. Although the acceleration of the BDC is qualitatively robust across the estimates, there is a large spread in the pattern of the trends. The annual mean trends are mainly (but not only) associated with DJF trends, and during this season we find consistent increasing wave drag (EP flux convergence) in both hemispheres in the three reanalyses (Figures 15a and 15b). The changes in lower stratospheric wave drag appear to be linked to ozone depletion in the SH polar stratosphere and to a more perturbed winter polar vortex in the NH after 1998. While DJF dominates the extratropical BDC trends in the lower stratosphere, the trends in tropical mean upwelling are most consistent in SON (Figure 12). The corresponding global trends suggest that the increase in upwelling in SON is at least partly linked to changes in the deep branch of the BDC driven by strengthened upper stratosphere forcing in both hemispheres (Figures 15c and 15d).

Our results regarding the long-term (1979–2012) acceleration of the BDC provide further support to recent works based on observations and reanalyses which obtained negative AoA trends in the lower stratosphere for similar periods [*Diallo et al.*, 2012; *Ray et al.*, 2014; *Ploeger et al.*, 2015b]. Nevertheless, these works also show slightly positive trends in AoA above 25 km (~30 hPa) in the NH extratropics, in agreement with the results of *Engel et al.* [2009]. This feature is not observed in the present work, at least not consistently across the estimates (see Figure 14). However, as mentioned in the section 1, the AoA trends might be affected by changes in mixing in addition to the advective circulation. In the recent work of *Ploeger et al.* [2015b] the effects of advection and mixing on the AoA acceleration are evaluated separately, and it is argued that mixing mainly drives the increase in AoA in this region.

Overall the present work demonstrates that, despite the large uncertainties in the evaluation of the BDC from reanalyses highlighted by the joint analysis of several estimates, relevant common features can be observed regarding the interannual variability and the trends in the lower and middle stratosphere.

Acknowledgments

The authors are thankful to the Editor and to the three reviewers for constructive comments. M. Abalos was mainly funded by the project StraDyVariUS of the French National Research Agency (ANR-13-BS06-0011) and by a postdoctoral grant from the Ecole Normale Supérieure de Paris. We acknowledge additional support from the EU 7th framework Program under grant 603557 (StratoClim). The JRA-55 data were downloaded from the NCAR CISL-RDA server (http://rda.ucar.edu), MERRA from the NASA MIRADOR portal (http://mirador.gsfc.nasa.gov/), and EI from the ECMWF Data Server (http://apps.ecmwf.int/datasets/).

References

Abalos, M., W. J. Randel, and E. Serrano (2012), Variability in upwelling across the tropical tropopause and correlations with tracers in the lower stratosphere, *Atmos. Chem. Phys.*, *12*, 11,505–11,517, doi:10.5194/acp-12-11505-2012.

Andrews, D. G., J. R. Holton, and C. B. Leovy (1987), *Middle Atmosphere Dynamics*, Academic Press, San Diego, Calif.

Austin, J., and F. Li (2006), On the relationship between the strength of the Brewer-Dobson circulation and the age of stratospheric air, *J. Geophys. Res.*, *33*, L17807, doi:10.1029/2006GL026867.

Baldwin, M. P., et al. (2001), The quasi-biennial oscillation, *Rev. Geophys.*, *39*(2), 179–229, doi:10.1029/1999RG000073.

Butchart, N., et al. (2010), Chemistry-climate model simulations of twenty-first century stratospheric climate and circulation changes, *J. Clim.*, *23*, 5349–5374, doi:10.1175/2010JCLI3404.1.

Butchart, N., et al. (2010), Chapter 4: Stratospheric dynamics, *CCMVal SPARC Rep. 5, WCRP–132, WMO/TD, 1526*, edited by V. Erying, T. Shepherd, and D. Waugh.

Butchart, N. (2014), The Brewer-Dobson circulation, *Rev. Geophys.*, *52*, 157–184, doi:10.1002/2013RG000448.

Calvo, N., R. R. Garcia, W. J. Randel, and D. R. Marsh (2010), Dynamical mechanism for the increase in tropical upwelling in the lowermost tropical stratosphere during warm ENSO events, *J. Atmos. Sci.*, *67*, 2331–2340, doi:10.1175/2010JAS3433.1.

Charlton, A. J., and L. M. Polvani (2007), A new look at stratospheric sudden warmings. Part I: Climatology and modeling benchmarks, *J. Clim.*, *20*, 449–469, doi:10.1175/JCLI3996.1.

Davis, S. M., C. K. Liang, and K. H. Rosenlof (2013), Interannual variability of tropical tropopause layer clouds, *Geophys. Res. Lett.*, *40*, 2862–2866, doi:10.1002/grl.50512.

Dee, D. P., et al. (2011), The ERA-interim reanalysis: Configuration and performance of the data assimilation system, *Q. J. R. Meteorol. Soc.*, *137*, 553–597, doi:10.1002/qj.828.

Diallo, M., B. Legras, and A. Chédin (2012), Age of stratospheric air in the ERA-Interim, *Atmos. Chem. Phys.*, *12*, 12,133–12,154, doi:10.5194/acp-12-12133-2012.

Ebita, A., et al. (2011), The Japanese 55-year Reanalysis JRA-55: An interim report, *SOLA*, *7*, 147–152, doi:10.2151/sola.2011-038.

Engel, A., et al. (2009), Age of stratospheric air unchanged within uncertainties over the past 30 years, *Nat. Geosci.*, *2*, 28–31, doi:10.1038/ngeo388.

Eyring, V., et al. (2006), Assessment of temperature, trace species, and ozone in chemistry-climate model simulations of the recent past, *J. Geophys. Res.*, *111*, D22308, doi:10.1029/2006JD007327.

Fueglistaler, S., B. Legras, A. Beljaars, J. J. Morcrette, A. Simmons, A. M. Tompkins, and S. Uppala (2009), The diabatic heat budget of the upper troposphere and lower/mid stratosphere in ECMWF reanalysis, *Q. J. R. Meteorol. Soc.*, *135*, 21–37, doi:10.1002/qj.361.

Fueglistaler, S., M. Abalos, T. J. Flannaghan, P. Lin, and W. J. Randel (2014), Variability and trends in dynamical forcing of tropical lower stratospheric temperatures, *Atmos. Chem. Phys.*, *14*, 13,381–13,412, doi:10.5194/acpd-14-13381-2014.

Garcia, R. R., and W. J. Randel (2008), Acceleration of the Brewer-Dobson circulation due to increases in greenhouse gases, *J. Atmos. Sci.*, *65*, 2731–2739, doi:10.1175/2008JAS2712.1.
Garcia, R. R., D. R. Marsh, D. E. Kinnison, B. A. Boville, and F. Sassi (2007), Simulation of secular trends in the middle atmosphere, *J. Geophys. Res.*, *112*, D09301, doi:10.1029/2006JD007485.
Garcia, R. R., W. J. Randel, and D. E. Kinnison (2011), On the determination of age of air trends from atmospheric trace species, *J. Atmos. Sci.*, *68*, 139–154, doi:10.1175/2010JAS3527.1.
Garny, H., M. Dameris, W. J. Randel, G. E. Bodeker, and R. Deckert (2011), Dynamically forced increase of tropical upwelling in the lower stratosphere, *J. Atmos. Sci.*, *68*, 1214–1233, doi:10.1175/2011JAS3701.1.
Gillett, N., and D. W. J. Thompson (2003), Simulation of recent Southern Hemisphere climate change, *Science*, *302*, 273–275, doi:10.1126/science.1087440.
Graf, H.-F., Q. Li, and M. A. Giorgetta (2007), Volcanic effects on climate: Revisiting the mechanisms, *Atmos. Chem. Phys.*, *7*, 4503–4511, doi:10.5194/acp-7-4503-2007.
Hall, T. M., and R. A. Plumb (1994), Age as a diagnostic of stratospheric transport, *J. Geophys. Res.*, *99*, 1059–1070, doi:10.1029/93JD03192.
Haynes, P. H., C. J. Marks, M. E. McIntyre, T. G. Shepherd, and K. P. and Shine (1991), On the "downward control" of extratropical diabatic circulations by eddy-induced mean zonal forces, *J. Atmos. Sci.*, *48*, 651–678.
Iwasaki, T., H. Hamada, and K. Miyazaki (2009), Comparisons of Brewer-Dobson circulations diagnosed from reanalyses, *J. Meteorol. Soc. Jpn.*, *87*, 997–1006, doi:10.2151/jmsj.87.997.
Kobayashi, S., et al. (2015), The JRA-55 reanalysis: General specifications and basic characteristics, *J. Meteorol. Soc. Jpn.*, *93*, 5–48, doi:10.2151/jmsj.2015-001.
Lamarque, J.-F., and S. Solomon (2010), Impact of changes in climate and halocarbons on recent lower stratosphere, *J. Atm. Sci.*, *23*, 2599–2611, doi:10.1175/2010JCLI3179.1.
Li, F., et al. (2012), Long-term changes in stratospheric age spectra in the 21st century in the Goddard Earth Observing System Chemistry-Climate Model (GEOSCCM), *J. Geophys. Res.*, *117*, D20119, doi:10.1029/2012JD017905.
McCormick, M. P., and R. E. Veiga (1992), SAGE II measurements of early Pinatubo aerosols, *Geophys. Res. Lett.*, *19*(2), 155–158, doi:10.1029/91GL02790.
McLandress, C., A. I. Jonsson, D. A. Plummer, M. C. Reader, J. F. Scinocca, and T. G. Shepherd (2010), Separating the dynamical effects of climate change and ozone depletion. Part I: Southern Hemisphere stratosphere, *J. Clim.*, *23*, 5002–5020, doi:10.1175/2010JCLI3586.1.
Monge-Sanz, B. M., M. P. Chipperfield, A. J. Simmons, and S. M. Uppala (2007), Mean age of air and transport in a CTM: Comparison of different ECMWF analyses, *Geophys. Res. Lett.*, *34*, L04801, doi:10.1029/2006GL028515.
Monge-Sanz, B. M., M. P. Chipperfield, D. P. Dee, A. J. Simmons, and S. M. Uppala (2013), Improvements in the stratospheric transport achieved by a chemistry transport model with ECMWF (re)analyses: Identifying effects and remaining challenges, *Q. J. R. Meteorol. Soc.*, *139*, 654–673, doi:10.1002/qj.1996.
Murgatroyd, R. J., and F. Singleton (1961), Possible meridional circulations in the stratosphere and mesosphere, *Q. J. R. Meteorol. Soc.*, *87*, 125–135, doi:10.1002/qj.49708737202.
Oman, L., D. W. Waugh, S. Pawson, R. S. Stolarski, and P. A. Newman (2009), On the influence of anthropogenic forcings on changes in the stratospheric mean age, *J. Geophys. Res.*, *114*, D03105, doi:10.1029/2008JD010378.
Ploeger, F., M. Abalos, T. Birner, P. Konopka, B. Legras, R. Müller, and M. Riese (2015b), Quantifying the effects of mixing and residual circulation on trends of stratospheric mean age of air, *Geophys. Res. Lett.*, *42*, 2047–2054, doi:10.1002/2014GL062927.
Plumb, R. A. (2002), Stratospheric transport, *J. Meteorol. Soc. Jpn.*, *80*, 793–809, doi:10.2151/jmsj.80.793.
Polvani, L. M., D. W. Waugh, G. J. P. Correa, and S.-W. Son (2011), Stratospheric ozone depletion: The main driver of twentieth-century atmospheric circulation changes in the Southern Hemisphere, *J. Clim.*, *24*, 795–812, doi:10.1175/2010JCLI3772.1.
Ramaswamy, V., et al. (2001), Stratospheric temperature trends: Observations and model simulations, *Rev. Geophys.*, *39*(1), 71–122, doi:10.1029/1999RG000065.
Randel, W. J., and A. M. Thompson (2011), Interannual variability and trends in tropical ozone derived from SAGE II satellite data and SHADOZ ozonesondes, *J. Geophys. Res.*, *116*, D07303, doi:10.1029/2010JD015195.
Randel, W. J., R. R. Garcia, and F. Wu (2002), Time-dependent upwelling in the tropical lower stratosphere estimated from the zonal-mean momentum budget, *J. Atmos. Sci.*, *59*, 2141–2152, doi:10.1175/1520-0469(2002)059<2141:TDUITT>2.0.CO;2.
Randel, W. J., R. R. Garcia, and F. Wu (2008), Dynamical balances and tropical stratospheric upwelling, *J. Atmos. Sci.*, *65*, 3584–3595, doi:10.1175/2008JAS2756.1.
Randel, W. J., et al. (2009), An update of observed stratospheric temperature trends, *J. Geophys. Res.*, *114*, D02107, doi:10.1029/2008JD01042.
Ray, E. A., et al. (2010), Evidence for changes in stratospheric transport and mixing over the past three decades based on multiple data sets and tropical leaky pipe analysis, *J. Geophys. Res.*, *115*, D21304, doi:10.1029/2010JD014206.
Ray, E. A., et al. (2014), Improving stratospheric transport trend analysis based on SF_6 and CO_2 measurements, *J. Geophys. Res. Atmos.*, *119*, 14,110–14,128, doi:10.1002/2014JD021802.
Rienecker, M. M., et al. (2011), MERRA: NASA's Modern-Era Retrospective Analysis for Research and Applications, *J. Clim.*, *24*, 3624–3648, doi:10.1175/JCLI-D-11-00015.1.
Rood, R. B. (2003), Reanalysis, in *Data Assimilation for the Earth System*, vol. 26, edited by Swinbank et al., pp. 361–372, Kluwer Acad. Publ., Netherlands.
Schoeberl, M. R., A. R. Douglass, R. S. Stolarski, S. Pawson, S. E. Strahan, and W. Read (2008), Comparison of lower stratospheric tropical mean vertical velocities, *J. Geophys. Res.*, *113*, D24109, doi:10.1029/2008JD010221.
Seidel, D. J., N. P. Gillett, J. R. Lanzante, K. P. Shine, and P. W. Thorne (2011), Stratospheric temperature trends: Our evolving understanding, *WIREs Clim. Change*, *2*, 592–616, doi:10.1002/wcc.125.
Seviour, W. J. M., N. Butchart, and S. C. Hardiman (2011), The Brewer-Dobson circulation inferred from ERA-Interim, *Q. J. R. Meteorol. Soc.*, *138*, 878–888, doi:10.1002/qj.966.
Shepherd, T. G. (2007), Transport in the middle atmosphere, *J. Meteorol. Soc. Jpn.*, *85*, 165–191.
Shepherd, T. G., and C. McLandress (2011), A robust mechanism for strengthening of the Brewer-Dobson circulation in response to climate change: Critical-layer control of subtropical wave breaking, *J. Atmos. Sci.*, *68*, 784–797, doi:10.1175/2010JAS3608.1.
Simmons, A. J., P. Poli, D. P. Dee, P. Berrisford, H. Hersbach, S. Kobayashib, and C. Peubeya (2014), Estimating low-frequency variability and trends in atmospheric temperature using ERA-Interim, *Q. J. R. Meteorol. Soc.*, *140*, 329–353, doi:10.1002/qj.2317.
Son, S.-W., L. M. Polvani, D. W. Waugh, H. Akiyoshi, R. Garcia, D. Kinnison, S. Pawson, E. Rozanov, T. G. Shepherd, and K. Shibata (2008), The impact of stratospheric ozone recovery on the Southern Hemisphere westerly jet, *Science*, *320*(5882), 1486–1489, doi:10.1126/science.1155939.

Son, S.-W., et al. (2010), Impact of stratospheric ozone on Southern Hemisphere circulation change: A multimodel assessment, *J. Geophys. Res.*, *115*, D00M07, doi:10.1029/2010JD014271.

Stiller, G. P., et al. (2012), Observed temporal evolution of global mean age of stratospheric air for the 2002 to 2010 period, *Atmos. Chem. Phys.*, *12*, 3311–3331, doi:10.5194/acp-12-3311-2012.

Thompson, D. W. J., and S. Solomon (2002), Interpretation of recent Southern Hemisphere climate change, *Science*, *296*(895), doi:10.1126/science.1069270.

Young, P. J. A. H. B., N. Calvo, L. Haimberger, P. J. Kushner, D. R. Marsh, W. J. Randel, and K. H. Rosenlof (2013), Agreement in late twentieth century Southern Hemisphere stratospheric temperature trends in observations and CCMVal-2, CMIP3, and CMIP5 models, *J. Geophys. Res. Atmos.*, *118*, 605–613, doi:10.1002/jgrd.50126.

von Storch, H., and F. W. Zwiers (1999), *Statistical Analysis in Climate Research*, 494 pp., Cambridge Univ. Press, Cambridge, U. K.

Wallace, J. M., R. L. Panetta, and J. Estberg (1993), Representation of the equatorial stratospheric quasi-biennial oscillation in EOF phase space, *J. Atmos. Sci.*, *50*(12), 1751–1762.

Waugh, D. (2009), The age of stratospheric air, *Nat. Geosci.*, *2*, 14–16, doi:10.1038/ngeo397.

Waugh, D. W., and T. M. Hall (2002), Age of stratospheric air: Theory, observations and models, *Rev. Geophys.*, *40*(4), 1010, doi:10.1029/2000RG000101.

Waugh, D. W., W. J. Randel, S. Pawson, P. A. Newman, and E. R. Nash (1999), Persistence of the lower stratospheric polar vortices, *J. Geophys. Res*, *104*, 27,191–27,201, doi:10.1029/1999JD900795.

Wolter, K., and M. S. Timlin (1998), Measuring the strength of ENSO—How does 1997/98 rank?, *Weather*, *53*, 315–324, doi:10.1002/j.1477-8696.1998.tb06408.x.

Wright, J. S., and S. Fueglistaler (2013), Large differences in reanalyses of diabatic heating in the tropical upper troposphere and lower stratosphere, *Atmos. Chem. Phys.*, *13*, 9565–9576, doi:10.5194/acp-13-9565-2013.